



HAL
open science

The efficiency of thermal fatigue in regolith generation on small airless bodies

Charles El Mir, K T Ramesh, Marco Delbo

► **To cite this version:**

Charles El Mir, K T Ramesh, Marco Delbo. The efficiency of thermal fatigue in regolith generation on small airless bodies. *Icarus*, 2019, 333, pp.356-370. 10.1016/j.icarus.2019.06.001 . hal-03053289

HAL Id: hal-03053289

<https://hal.science/hal-03053289v1>

Submitted on 10 Dec 2020

HAL is a multi-disciplinary open access archive for the deposit and dissemination of scientific research documents, whether they are published or not. The documents may come from teaching and research institutions in France or abroad, or from public or private research centers.

L'archive ouverte pluridisciplinaire **HAL**, est destinée au dépôt et à la diffusion de documents scientifiques de niveau recherche, publiés ou non, émanant des établissements d'enseignement et de recherche français ou étrangers, des laboratoires publics ou privés.

The efficiency of thermal fatigue in regolith generation on small airless bodies

Charles El Mir^a, KT Ramesh^{a,b,c}, Marco Delbo^d

^a*Department of Mechanical Engineering, The Johns Hopkins University, Baltimore, Maryland, 21218*

^b*Department of Earth and Planetary Sciences, The Johns Hopkins University, Baltimore, Maryland 21218*

^c*Hopkins Extreme Materials Institute, The Johns Hopkins University, Baltimore, Maryland, 21218*

^d*Université Côte d'Azur, Observatoire de la Côte d'Azur, CNRS, Laboratoire Lagrange, Boulevard de l'Observatoire-CS 34229, 06304 Nice Cedex 4, France*

Abstract

Regolith generation by thermal fatigue has been identified as a dominant mechanism for the breakdown of small (cm-sized) rocks on certain airless bodies. Simple numerical models for thermal fatigue seemed to indicate that this breakdown occurs faster in the larger decimeter-sized rocks, which is in contrast to the predictions of disruption models through successive micrometeorite impacts. The observation is justified by the existence of larger temperature gradient in bigger rocks, but it is not clear that this conclusion can be extrapolated or scaled to meter-sized boulders. Here we reveal a transition in the rock disaggregation rates by thermal fatigue when rock sizes rise above a critical length scale. A simple analytic model is formulated to predict the time to fracture of rocks on small airless bodies. We consider an uncoupled approach consisting of a one-dimensional thermal model, and a two-dimensional fracture model. The solution of the heat equation is used as input to the thermomechanical crack growth problem. This new

understanding could provide bounds on the survival rates of asteroidal rocks, and may help in coupling thermal fatigue with a mechanical disruption model to obtain a multi-mechanism view of regolith evolution in the solar system.

1. Introduction

Asteroids, comets, and small planets in the solar system are covered with a layer of loose and unconsolidated rocks called regolith. Surface imagery acquired by space probes has indicated that even the relatively small kilometer-sized asteroids carry a complex blanket of fine rocks smaller than a few centimeters. Images of asteroid (25143) Itokawa (Murdoch et al., 2015) and comet 67P/Churyumov-Gerasimenko (El-Maarry et al., 2015) highlighted the existence of freshly exposed boulder surfaces, indicating that the evolution of these boulders is driven by an active surface rejuvenation process that could differ from those manifested on the lunar surface (Veverka et al., 2001b).

It is generally accepted that the lunar regolith is the byproduct of a long history of mechanical disruption wherein large boulders are eroded by a series of micro- and macro-meteoritic impacts (Gault et al., 1974). The abundance of impact-induced agglutinates points towards the dominant role that meteoritic impact had on the evolution of the lunar regolith. However, on small asteroids, the ejecta velocities from an impact event typically exceed the asteroid's escape velocity, and most of the resulting small debris would be lost into space as opposed to being reaccumulated on the surface (Housen et al., 1979). Early models of impact-induced regolith on airless bodies indicated that small asteroids (10 km or smaller) should only retain a negligible regolith layer (Housen et al., 1979; Housen and Wilkening, 1982; Pettengill

22 and Jurgens, 1979). Consequently, asteroidal regolith generation remained,
23 for the most part, a poorly understood mechanism (Melosh, 2011).

24 Recently, thermal fatigue was suggested as a mechanism for in-place rock
25 breakdown capable of generating fine-scaled regolith layers without any sub-
26 sequent ejection. Observational evidence in favor of thermal fatigue in the
27 solar system includes the work of Eppes et al. (2015) who collected orienta-
28 tion measurements from more than 1,800 cracks visible in nearly 1,500 rocks
29 photographed by the Spirit rover during its journey on the Martian surface.
30 Their measurements showed that these cracks exhibit preferred orientations
31 consistent with solar-induced thermal stresses. Dombard et al. (2010) also
32 showed that some boulders inside regolith “ponds” on 433 Eros have debris
33 aprons, which were interpreted as the evidence that these rocks erode in
34 place, likely due to thermal cracking. In another work, Delbo et al. (2014)
35 examined fragmentation induced by the diurnal temperature variations on
36 asteroids. Their results indicated that thermal fatigue could play an impor-
37 tant role in the generation of fine-grain regolith on small asteroids, and that
38 the process is several orders of magnitudes faster than mechanical impact.
39 Delbo et al. (2014) also showed that thermal fatigue could break down larger
40 rocks faster than smaller ones, owing to the greater temperature gradients
41 in the bigger rocks—a trend that is in contrast to what is seen in the case
42 of mechanical disruption by microimpacts. This latter result provides an
43 explanation for the presence of fine regolith on small asteroids, but it is not
44 clear how it would apply for larger boulders (the Delbo et al. (2014) calcu-
45 lations were for surface rocks with diameters between 1 and 10 cm). The
46 presence of meter-sized rocks on several asteroids, such as those pictured on

47 Itokawa (Veveřka et al., 2001b; Saito et al., 2006), indicates that thermal
48 fatigue ought to behave differently at these larger sizes.

49 Here we demonstrate that thermal fatigue has an inherent lengthscale
50 that characterizes the bounds on the rate of fragmentation for rocks in the
51 range of 1–50 cm. We first develop a thermomechanical model that tracks the
52 evolution of a crack due to the diurnal temperature variations in an asteroidal
53 rock and efficiently bridges across the vastly different timescales of rotation
54 and time to fracture. Using the model, we compute the trends in the time-
55 to-fragmentation of sub-meter-sized rocks. We then develop a generalized
56 analytical expression to predict the survival times of regolith particles on
57 small airless bodies. Note that the regolith typically consists of rocks of a
58 wide range of sizes. Here we focus on rocks that are larger than a mm. The
59 rock breakdown study performed in this paper is limited to the aforemen-
60 tioned range of 1–50 cm, and it will be shown that thermal fatigue would be
61 most efficient for rocks of such diameters.

62 2. Numerical Modeling of Thermal Fatigue

63 Thermal fatigue cracking of rocks results from the fluctuations in the tem-
64 perature field that develop driving forces (which are not merely the stresses,
65 but rather the stress intensity factors at the crack tips) on cracks within
66 a rock. These cracks may then experience sub-critical fatigue growth until
67 fragmentation. In this section, we present a numerical framework that cal-
68 culates the crack tip driving forces due to thermal cycling and predicts crack
69 growth over a large number of cycles.

70 *2.1. Thermal Model*

71 We consider an uncoupled solution that allows us to solve the heat equa-
72 tion (solar radiation and conduction) first, and use the resultant temperature
73 field as an input to the thermomechanical deformation problem. Effectively,
74 we are assuming that the stress state does not affect the thermal properties
75 of the rocks and that the cracks have negligible effects on the temperature
76 field. The motivation for this assumption is that heat is conducted parallel
77 to the direction of the crack propagation. We recognize that the presence of
78 cracks affects the thermal conductivity of a rock, essentially in the direction
79 perpendicular to the crack plane.

80 The temperature profile in surface rocks is calculated using a diffusion
81 model based on the asteroid thermal model developed by Spencer et al.
82 (Spencer et al., 1989). This model calculates the temperature $T(t, z)$ as
83 function of time and depth in a rock at the equator of an asteroid by solving
84 the heat equation:

$$\rho C_p \frac{\partial T}{\partial t} = \kappa \frac{\partial^2 T}{\partial z^2}, \quad (1)$$

85 where κ is the thermal conductivity, C_p the heat capacity, ρ the density and
86 the coordinate z increases from zero at the surface downwards. Numeric
87 values for the parameters used in this study are given in Table 1. It is
88 documented that thermal conductivity varies with temperature, in particular
89 in the case of meteorites (Opeil et al., 2010, 2012). However, this effect is
90 small for the diurnal temperature variations considered in this study. Recent
91 astronomical observations showed this effect also in case of asteroids (Rozitis
92 et al. (2018); with some potential hints also observed on the asteroid 6 Hebe

93 by Marsset et al. (2017)). This effect is probably due to the heat conduc-
 94 tion in a regolith that is dominated by the radiative term, which is pro-
 95 portional to T^3 . For the case treated here concerning rocks where heat is
 96 essentially transported by the solid heat conduction, however, a temperature
 97 dependent thermal conductivity would only slightly enhance the maximum
 98 diurnal temperature variations by some degrees (as shown in Delbo et al.
 99 (2015)). Therefore, in this formulation we assume that the thermal properties
 100 do not depend on depth and temperature. As a consequence, the thermal
 101 cracking effects hereafter estimated are somewhat conservative. Given the
 102 uncertainties in all other thermo-mechanical parameters, we prefer to use the
 103 simpler model of temperature independent conductivity, which gives results
 104 that can be compared with other literature studies.

105 The heat diffusion equation is solved with the surface boundary condition
 106 of

$$\frac{(1 - A)S_{\odot}}{r^2}\mu(t) = \sigma_{rad} \epsilon_{ir}T^4|_{z=0} - \kappa \frac{\partial T}{\partial z}|_{z=0} \quad (2)$$

107 where: σ_{rad} is the Stefan-Boltzman constant; ϵ_{ir} the infrared emissivity,
 108 which is assumed to be equal 0.9 as common in studies of asteroid surfaces
 109 (see Delbo et al. (2015) and references therein); A is the bolometric Bond
 110 albedo, which is typically a few percent for the generally dark asteroid sur-
 111 faces, r is the heliocentric distance of the asteroid in au; and S_{\odot} is the solar
 112 constant at 1 AU of 1370 W m^{-2} . The parameter μ is related to the direction
 113 cosine between the normal to the surface element and the direction to the
 114 sun θ , with $\mu(t) = \cos[\theta(t)]$ for $-\pi/2 < \theta < \pi/2$ and $\mu(t) = 0$ otherwise. The
 115 angle θ represents the local day time of the surface element, i.e., $\theta = 2\pi/P$

116 where P is the rotation period of the asteroid. This boundary condition
117 implies that the **rock** is treated as a flat surface. It is known that surface
118 roughness affects the observed temperatures of airless bodies (Rozitis and
119 Green, 2011; Davidsson et al., 2015); however, this is a global effect on large
120 surfaces. Locally, roughness can enhance the dayside temperature of rocks on
121 the surface due to the mutual heating. This happens when a rock has a non-
122 zero view factor towards warm surface elements (i.e.: the rock experiences
123 local radiation due to the local topolgy), resulting in slightly larger temper-
124 ature excursion between day and night. The flat surface thermal model we
125 consider here is thus a conservative case.

126 At a depth of 5 meters, the additional boundary condition of $\frac{\partial T}{\partial z}|_{z=5m} = 0$
127 implies that there is no heat flow towards (or from) deeper into the body.
128 These are similar to the conditions imposed by classical asteroid thermal
129 modeling (see Delbo et al. (2015) for a review).

130 The resulting time-dependent and depth-dependent temperature fields for
131 rocks on the surface of a small carbonaceous chondritic near-Earth asteroid
132 having a rotational period of 6 hours are shown in Fig. 1. This is used as the
133 input to the computational model in Section 2.4.

134 In Fig. 1, the temperature as a function of depth during a 6 hour day/night
135 cycle is plotted at 15 min increments (changing hues from red to blue).
136 The **asteroid's** surface experiences the largest temperature changes, which
137 are quickly attenuated and disappear below a depth of 20 cm centimeters.
138 Notice that the temperature variations as a function of depth are highly
139 time-dependent, with the maxima being experienced at different times for
140 different depths. This highlights the need for an efficient thermomechanical

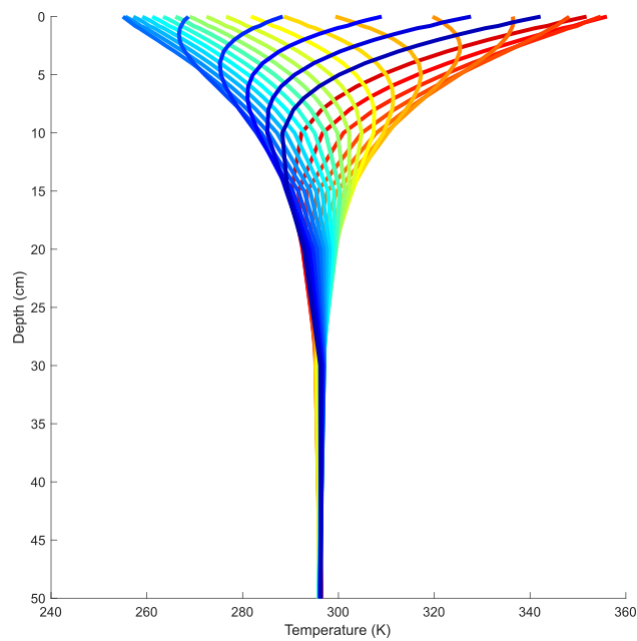


Figure 1: Temperature **in a rock at 1 AU** as a function of depth during a 6 hour day/night cycle, plotted at 15 min increments. This temperature profile is typical of diurnal thermal cycling. The heat wave attenuates quickly beyond the skin depth, and temperature variations become negligible.

141 model that can solve for the stress fields at small increments of times, while
142 being capable of tracking the crack growth for many years.

143 *2.2. Thermomechanical Crack Growth Model*

144 In this section, we develop a thermomechanical model that predicts the
145 fatigue crack growth in a rock as a result of the spatiotemporally varying
146 temperature field calculated in the thermal model (Section 2.1). To do this,
147 we must compute the driving force on a crack tip in the rock. This driving
148 force is called the stress intensity factor or SIF. It is important to recognize
149 that the stress field computed within an uncracked body does not identify
150 whether or not a crack will grow (Anderson, 2017), and indeed, an accurate
151 analysis of the stress field within an elastic rock containing a crack will always
152 show an infinite stress at the crack tip. Understanding crack growth requires
153 the use of the concepts of fracture mechanics. In general, cracks grow in
154 one of three modes, each of which has an associated stress intensity factor:
155 Mode I or tension, which results from tension perpendicular to the crack
156 faces, with stress intensity factor K_I ; Mode II or shear, which results from
157 shear stresses acting parallel to the crack faces and causing crack sliding,
158 with stress intensity factor K_{II} ; and Mode III or antiplane shear, which
159 results from shear displacements acting parallel to the crack front, with stress
160 intensity factor K_{III} . These stress intensity factors fully describe the stress,
161 strain and displacement functions at the crack tip, and crack growth laws
162 (crack direction, crack length and crack speed) are typically written in terms
163 of these quantities (S. M. Beden et al., 2009; Paris et al., 1999). Having
164 multiple modes active at one time is said to define a mixed-mode problem,
165 and the thermal fatigue problem turns out to be mixed mode. So, to model

166 the thermal fatigue fragmentation caused by the growth of a crack in a rock,
167 we must first compute the stress intensity factors as the temperature field is
168 varying.

169 *2.2.1. Background*

170 Stress intensity factors depend on both the loading configuration as well
171 as the geometry and crack size (Tada et al., 2000). Closed-form analytical so-
172 lutions only exist for some simple idealized cases such as remote tension on a
173 cracked plate. Some “universal” weight function approaches have also been
174 developed (Glinka and Shen, 1991) but their application remains limited,
175 especially with increasing complexity in loading profiles and crack config-
176 urations. Consequently, numerical approaches such as the Finite Element
177 Method (or its extensions) are often needed. While traditional finite element
178 method formulations are not capable of capturing the discontinuity in the
179 displacement field that is caused by the presence of a crack, some measure
180 of the singularity at the crack tip can still be achieved by explicitly meshing
181 a sharp notch as part of the shape model. Post-processing techniques can
182 then be used to estimate the stress intensity factor either by fitting the dis-
183 placement or stress field solutions to the near-crack analytical solution, or
184 by means of an energy integral approach (Chan et al., 1970). However, the
185 post-processing approach requires an increasingly fine mesh near the notch
186 to obtain satisfactory results, which increases the computational cost and
187 data preparation effort for each simulation.

188 As a consequence, numerical approaches that extend the traditional finite
189 element method have been developed for modeling cracked bodies. These are
190 often achieved by formulating special types of elements that include a singu-

191 larity in their shape functions (Blackburn, 1973; Benzley, 1974; Nash Gifford
192 and Hilton, 1978) and using them near the notch to reduce the required
193 amount of fine-meshing. Other methods include the quarter-point finite ele-
194 ment (Henshell and Shaw, 1975; Barsoum, 1976), the boundary collocation
195 method (Bowie and Neal, 1970; Newman, 1971), and the boundary elements
196 method (Alarcon et al., 1978; Cruse, 1988). These techniques can reasonably
197 capture the singularity for a stationary crack tip. However, any crack propa-
198 gation would then require the regeneration of a new mesh that conforms with
199 the new crack geometry. This “remeshing” step is often the most computa-
200 tionally expensive step in an analysis, making these methods less suitable for
201 crack evolution simulations.

202 One technique to avoid this remeshing step is the so-called eXtended
203 Finite Element Method (XFEM) (Belytschko and Black, 1999; Karihaloo
204 and Xiao, 2003). Belytschko and Black (1999) first introduced XFEM by
205 discretizing a crack in the mesh through the enrichment (provision of ad-
206 ditional degrees of freedom) of elements near the crack tip and crack faces.
207 The enrichments exploit the partition of unity property inherent in finite el-
208 ements (Melenk and Babuška, 1996) to include the asymptotic displacement
209 field resulting from the crack without modifying the existing mesh. Moës
210 et al. (1999) then introduced the generalized Heaviside step function to char-
211 acterize the discontinuous field across the crack faces away from the crack
212 tip, and Daux et al. (2000) detailed a procedure for multiple branched cracks
213 through the use of a junction function.

214 In XFEM, cracks can be incorporated into an existing finite element mesh
215 by first identifying the elements that contain the crack, and labeling their

216 respective nodes as face-enriched nodes related to elements that are split by
217 a crack, or tip-enriched nodes related to elements containing a crack tip (see
218 Fig. 2). Cracks can then move freely within the mesh without requiring a
219 reconstruction of the mesh itself, but rather a simple identification of the ele-
220 ments to be “enriched” with additional degrees of freedom. The displacement
221 field can then be computed using the standard finite element solvers (Bathe,
222 2014). The stress intensity factor is then calculated in the post-processing
223 stage using an interaction integral method (Nash Gifford and Hilton, 1978;
224 Wilson and Yu, 1979).

225 *2.2.2. Model Details*

226 Here, we develop a custom XFEM implementation (based on Bordas et al.
227 (2007)) that solves for the displacement field in cracked rocks subjected to
228 cyclic thermal loading. Since the near-surface temperature variations change
229 quickly with time (see Fig. 1), the model is optimized to efficiently bridge be-
230 tween the relatively small timesteps within a single period of rotation (using
231 15-minute increments) and the longer timescale of fragmentation ($10^3 - 10^6$
232 years).

233 Consider a cracked rock that is thermally cycled. We idealize the rocks as
234 plane strain cylindrical 2D bodies. First, a representative mesh of the geome-
235 try (circular in our case) is generated irrespective of the cracks. Then, cracks
236 are overlaid on the mesh, and the elements that are split by a crack and those
237 that contain crack tips are identified (Fig. 2). These elements are “enriched”
238 with the additional degrees of freedom, so that the total displacement field
239 u at a point x is written in terms of the regular FEM displacement (without
240 a crack) and an XFEM displacement (related to the crack enrichments):

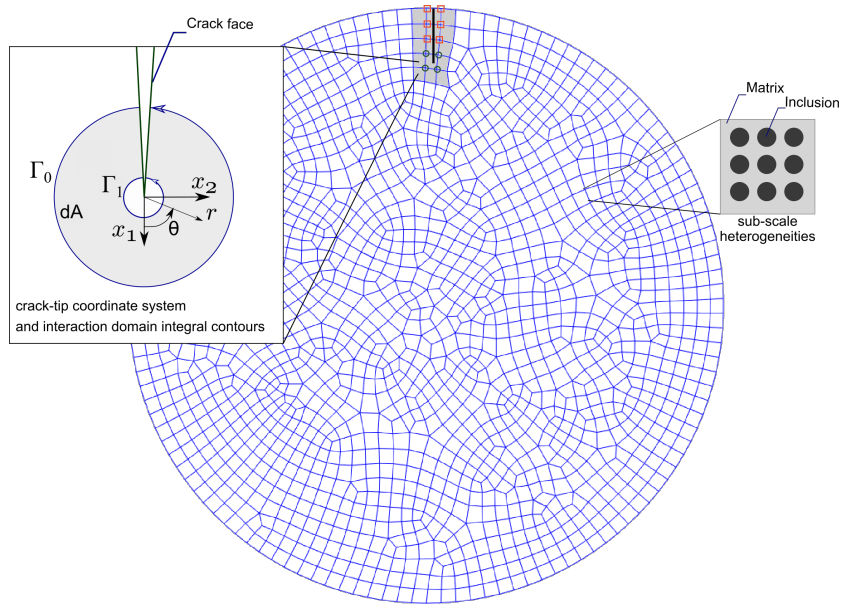


Figure 2: Mesh of a circular rock containing a surface crack. The gray-shaded elements are directly affected by the crack and will include additional shape functions (degrees of freedom). The nodes identified with a red square belong to elements that are “split” by the crack and will contain step-function enriched degrees of freedom. The nodes labeled with a green circle belong to the element that contains the crack tip and will be enriched with asymptotic functions to capture the singularity at the crack tip. Each element contains a sub-scale distribution of heterogeneities (inset on the right), which are assumed to be circular and distributed in a regular array. These inclusions will contribute to the global stress tensor. The left inset presents the crack-tip coordinate system and the domains for the interaction contour integral used to calculate the stress intensity factor. On the mesh, these contours span 3–5 elements around the crack tip. Symbols are defined in the subsequent pages of the main text.

$$u(x) = \underbrace{\sum_i N_i(x) \hat{u}_i}_{u^{FEM}} + \underbrace{\sum_j N_j(x) \psi(x) a_j}_{u^{XFEM}} \quad (3)$$

241 where \hat{u} is the nodal displacement from traditional finite element formulation,
 242 N the finite element shape function, the a_j 's are the additional degrees of free-
 243 dom related to the enrichment ψ that is asymptotic for crack tip enrichment
 244 (Williams, 1961) and a Heaviside step-function for crack face enrichment.

245 The temperature field induces thermal strains, which are captured through
 246 additional nodal forces given for a unit thickness as:

$$\mathbf{f}^{th} = \int_A \mathbf{BC} \boldsymbol{\epsilon}^{th} dA = \int_A \mathbf{BC} (\boldsymbol{\alpha} \Delta T) \mathbf{I} dA \quad (4)$$

247 with \mathbf{B} being the displacement differentiation matrix, \mathbf{C} the stiffness tensor,
 248 $\boldsymbol{\epsilon}^{th}$ the thermal part of the total strain, $\boldsymbol{\alpha}$ the thermal expansion coefficients,
 249 and \mathbf{I} the identity tensor.

250 Thereafter, the global stiffness matrix and the force vectors are con-
 251 structed in the same manner as the traditional finite element method (Reddy,
 252 2006). The nodal displacements are then obtained using an implicit solver,
 253 and the gradients of the displacement field gives the total strain tensor $\boldsymbol{\epsilon}$.
 254 The Cauchy stress tensor ($\boldsymbol{\sigma}$) is computed from the mechanical strain $\boldsymbol{\epsilon}^m$,
 255 using the linear constitutive relation:

$$\boldsymbol{\sigma} = \mathbf{C} : \boldsymbol{\epsilon}^m = \mathbf{C} : (\boldsymbol{\epsilon} - \boldsymbol{\epsilon}^{th}) \quad (5)$$

256 Asteroidal rocks contain inclusions with varying thermomechanical prop-
 257 erties. The mismatch in thermal expansion coefficients between inclusion

258 and matrix generates additional internal stresses as the matrix constrains
 259 the grain's expansion. An analogous behavior is often observed in composite
 260 materials subjected to high temperature variations (Evans, 1974; Biernacki
 261 et al., 1999; Ajaja and Barthelat, 2016). Our model is also capable of treat-
 262 ing inclusions as heterogeneities that are part of the material mesh, but such
 263 analysis will not be addressed in this paper. In this work, the inclusions are
 264 treated as sub-scale (Fig. 2) to our mesh resolution. The effective contribu-
 265 tion of the thermal expansion mismatch stress caused by a volume fraction f
 266 of inclusions is accounted for using a representative volume element approach
 267 following a modified Eshelby formulation (Hsueh and Becher, 1996) as:

$$\boldsymbol{\sigma}^{TM} = \left(\frac{1 - 2\nu_{inc}}{E_{inc}} + \frac{1}{1 - f} \frac{1 + \nu_m}{2E_m} + \frac{f}{1 - f} \frac{1 - 2\nu_m}{E_m} \right)^{-1} (\boldsymbol{\alpha}_m - \boldsymbol{\alpha}_{inc}) \Delta T \mathbf{I} \quad (6)$$

268 where E and ν are the Young's modulus and Poisson ratio, respectively. The
 269 subscript m refers to the matrix (or bulk) material properties, and inc refers
 270 to properties of the average inclusion (such as a chondrule).

271 Now that we have the displacements, strains, and stresses, we can com-
 272 pute the stress intensity factor at the crack tip. Typically, the energy release
 273 rate at the crack tip (which is related to the stress intensity factor) can be
 274 extracted by means of a J-integral approach (Rice, 1968). The J-integral is
 275 a path-independent line integral that is equal to zero for a simply connected
 276 closed loop around a region containing no singularities. When the integral
 277 path contains a crack, the J-integral is equal to the energy release rate for the
 278 crack growth, which is related to the stress intensity factor at the crack tip.

279 Note that the J-integral alone does not provide enough information to ex-
 280 tract the individual measures of K_I and K_{II} in a mixed-mode crack problem,
 281 since it depends on their combined effects:

$$J = \frac{(K_I^2 + K_{II}^2)}{E^*} \quad (7)$$

282 where E^* is equal to the Young's modulus at the crack tip E for plane stress,
 283 and $E^* = E/(1 - \nu^2)$ for plane strain, with ν the Poisson's ratio at the crack
 284 tip. Note that K_{III} is not relevant for these 2D problems.

285 In this work, we use the interaction integral approach (Yau et al., 1980;
 286 Belytschko and Black, 1999), which decouples the individual contributions of
 287 K_I and K_{II} by superposing the solution of assumed "auxiliary" fields (note
 288 that the linearity of the elastic problem implies that the superposition of two
 289 fields at equilibrium should lead to another equilibrium state). Proper choices
 290 of these auxiliary states allow for decoupling the K_I and K_{II} contributions.
 291 The J-integral for the superposed equilibrium state (superscript *sup* below)
 292 would contain contributions from the auxiliary state (superscript *aux* below)
 293 and the original state in XFEM (no superscript). That is:

$$J^{sup} = \frac{1}{E_{tip}^*} ((K_I + K_I^{aux})^2 + (K_{II} + K_{II}^{aux})^2) = J + J^{aux} + I^{sup} \quad (8)$$

294 The I^{sup} term is an interaction term that contains the coupling between
 295 the XFEM solution and the auxiliary field solution. It can be shown that
 296 I^{sup} is a line integral of the form:

$$I^{sup} = \lim_{\Gamma_1 \rightarrow 0} \oint (\sigma_{ij}^{aux} u_{j,1} + \sigma_{ij} u_{j,1}^{aux} - \sigma_{jk}^{aux} \epsilon_{jk} \delta_{1i}) m_i q d\Gamma_1 \quad (9)$$

297 where m_i are the components of the unit outward normal vector to the inte-
 298 grating contour Γ_1 (Fig. 2).

299 Recall that the fundamental property of the J-integral is that it equates
 300 to zero over a closed path away from the crack. However, Wilson and Yu
 301 (1979) showed that, in general, the integral is non-zero when thermal stresses
 302 are present, meaning that for thermal stress crack problems the crack tip
 303 stress intensity factors cannot be determined directly from such a line integral
 304 calculation. The alternate formulation of Wilson and Yu (1979) is used in our
 305 model after converting the line-integral into an equivalent domain integral
 306 (EDI) written in crack-tip coordinates (Merle and Dolbow, 2002; KC and
 307 Kim, 2008), as this is better suited for implementation in finite element codes
 308 since it is written in terms of quantities readily available from the analysis
 309 step:

$$I^{sup} = \int_A (\sigma_{ij}^{aux} u_{j,1} + \sigma_{ij} u_{j,1}^{aux} - \sigma_{jk} \epsilon_{jk} \delta_{1i}) q_i dA \\ + \int_A (\sigma_{ij}^{aux} \alpha(\Delta T)_{,1} \delta_{ij}) q dA \quad (10)$$

310 Here, q is a weight function with values varying smoothly from 1 on Γ_1 to 0
 311 on Γ_0 (Fig. 2). The second integral comes from the thermal contribution to
 312 the J-integral. The different stress intensity modes can now be individually
 313 extracted through the proper choice of auxiliary fields (Yau et al., 1980). It
 314 follows from Eq. (8) that the mixed-mode stress intensity factors are related

315 to the interaction integral as:

$$I^{sup} = \frac{2}{E^*} (K_I K_I^{aux} + K_{II} K_{II}^{aux}) \quad (11)$$

316 Then, by equating Eqs. (11) and (10) and using the fundamental solution
 317 (Sun and Jin, 2012) for a crack in pure mode-I ($K_I^{aux} = 1$, $K_{II}^{aux} = 0$), the K_{II}
 318 terms are dropped and we are left with K_I as the only unknown. Similarly,
 319 setting the auxiliary field to the pure mode-II solution ($K_I^{aux} = 0$, $K_{II}^{aux} = 1$)
 320 gives K_{II} .

321 Now that the mixed-mode stress intensity factors are known, we use an
 322 appropriate fatigue crack growth law to describe the rate of crack propagation
 323 after a thermal excursion cycle. We here use the so-called Paris' Law (Paris
 324 et al., 1999), which relates the crack length, a , in a given number of cycles,
 325 N , to the excursion in the effective stress intensity factor, ΔK_{eff} :

$$\frac{da}{dN} = C (\Delta K_{eff})^n \quad (12)$$

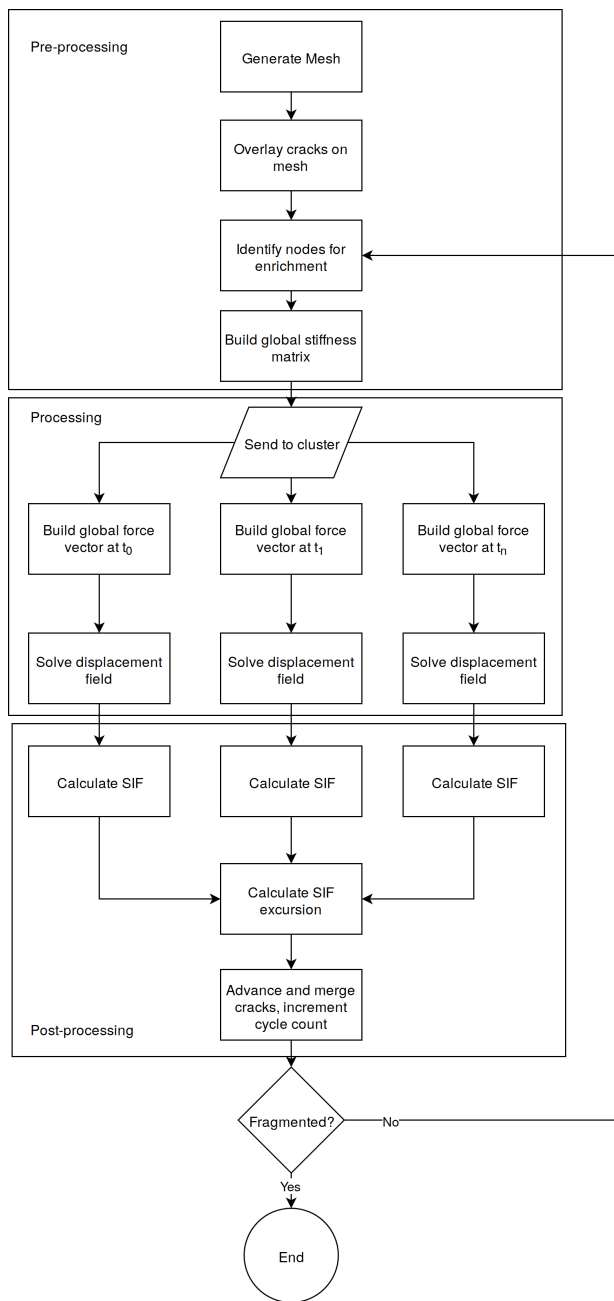
326 where C and n are material parameters fit to fatigue experiments. Note that
 327 these parameters generally depend on the material, environment, frequency,
 328 temperature, and loading. We use the energy release rate model (Rhee and
 329 Salama, 1987) to define the effective stress intensity factor, combining the
 330 K_I and K_{II} contributions:

$$K_{eff} = \sqrt{K_I^2 + K_{II}^2} \quad (13)$$

331 The crack is allowed to grow arbitrarily in the mesh, with an orientation
 332 determined by the maximum tangential stress criterion (Erdogan and Sih,

333 1963) given by:

$$\theta = 2 \arctan \left(\frac{1}{4} \frac{K_I}{K_{II}} \pm \frac{1}{4} \sqrt{\left(\frac{K_I}{K_{II}} \right)^2 + 8} \right) \quad (14)$$



1

Figure 3: Flowchart of the thermomechanical model developed in this work. The pre-processing stage sets up the rock geometry, thermomechanical properties, and initial conditions. The processing stage runs in parallel on multiple computational nodes to solve different timesteps within a single period of rotation. The excursion in stress intensity factor is calculated in the post-processing stage and used to advance cracks until fragmentation.

334 With these equations implemented into our model, we are able to perform
335 high-resolution simulations of thermal fatigue crack growth over multiple
336 cycles (see Fig. 3). We further optimize our algorithm to make use of multiple
337 processors, making it suitable to be run on high-performance computational
338 clusters. The computational “bottlenecks” of the XFEM algorithm in this
339 case arise from: a) assembling the global stiffness matrix and force vector,
340 b) solving the set of coupled linear equations, and c) detecting the nodes for
341 enrichment after cracks propagate. Therefore, we first parallelize the stiffness
342 matrix and force vector assembly process through an algorithm that maps
343 the element-wise contributions to their position in the global matrices. This
344 allows for resolving elements from different parts of the mesh onto separate
345 computational cores and populating their contribution to the global stiffness
346 matrix and force vector using the map. In addition, the temperature variation
347 in our thermal fatigue problem has no effect on the global stiffness matrix
348 during a single cycle (when the current crack has not yet propagated), and
349 only affects the global force vector (following Eq. (4)). So during a single step,
350 we only build the global stiffness matrix once and send the force vector for
351 each time increment onto a separate node for parallel computation (that is,
352 all time increments can be solved simultaneously on different computational
353 nodes; Fig. 3) using an efficient parallel implicit matrix solver (Witkowski
354 et al., 2015). When the crack propagates at the end of a thermal cycle, we
355 detect affected elements using a sub-grid search algorithm that starts from
356 elements surrounding the crack tip (instead of looping over all elements).
357 This typically reduces the search algorithm to a much smaller loop since the
358 fatigue crack growth distance in a single cycle rarely exceeds a few elements

359 from the original position. These features allow us to efficiently bridge across
360 a large number of cycles and makes our thermomechanical model effective
361 for modeling the thermal fatigue breakdown of rocks on airless bodies in the
362 solar system.

363 *2.3. Stresses in cracked rocks under thermal cycling*

364 We first discuss the stress fields that arise in a cracked rock as a result of
365 thermal cycling. As a typical example, Fig. 4 presents the computed stress
366 field in a 40 cm diameter rock containing a 15 cm crack. The figure shows
367 six snapshots (the columns) from the computations, one every hour over the
368 6 hour period. The top row shows the temperature field in the rock at that
369 time, and the bottom row shows the corresponding stress field in the cracked
370 rock. For comparison, the middle row shows the stress field that would exist
371 in the uncracked rock. The cracked rock has an entirely different stress field
372 than the uncracked rock, with different maximum stresses, and with these
373 maxima located in different parts of the rock. These differences highlight the
374 importance of using fracture-mechanics solutions to accurately capture the
375 singularity at the crack tip. Note that answering the question of *how much* a
376 crack will grow in such a thermal cycle can *only* be done by using the stress
377 intensity factor as a measure. Further, stresses alone cannot identify the
378 extent of crack growth. Thus the peak stresses obtained from an uncracked
379 rock alone are not reasonable indicators of the thermal fatigue lifespan of
380 cracked rocks.

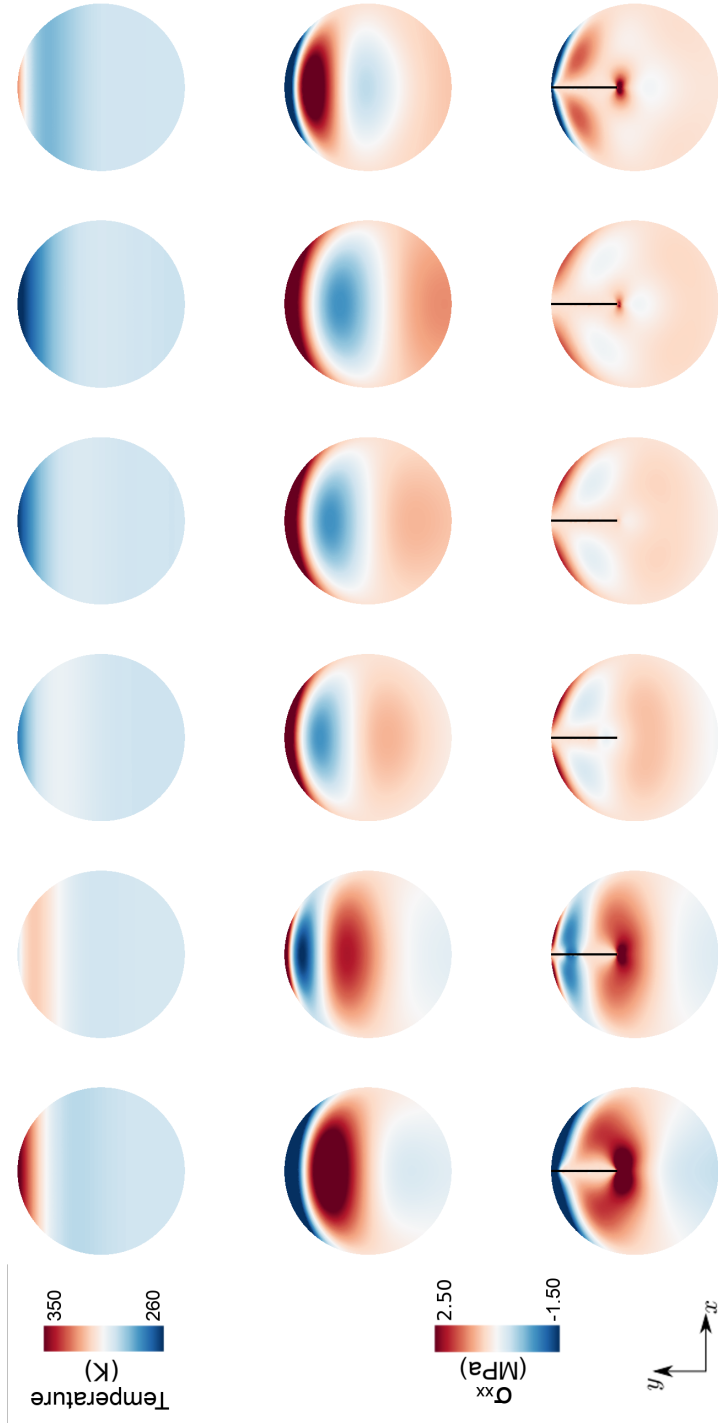


Figure 4: The temperature field in a 40 cm diameter rock is plotted in the first row at 1 hour increments for a 6 hour thermal cycle. The stress field perpendicular to the crack faces (stresses in the crack opening direction) is shown on the second and third rows. The second row is for a rock without any crack, while the third row shows the stress field in a rock of the same size that has a 15 cm surface crack. Notice that the stress at the crack tip is singular and that the crack relaxes the stress field at its faces.

381 *2.4. Rate of rock breakdown by thermal fatigue*

382 We now use the thermal and thermomechanical models presented so far
383 to determine the time required to fracture rocks of varying diameters through
384 the growth of a crack by thermal fatigue. We consider the case of a near-
385 Earth asteroid with a 6-hour period of rotation, which is typical of many
386 small asteroids (Gregersen, 2009). We model circular rocks of different di-
387 ameters, all containing an initial surface crack (see the mesh in Fig. 2 and
388 Fig. 8 in Delbo et al. (2014)). We use the thermomechanical properties for
389 carbonaceous chondrite (Table 1) and fatigue parameters of Carrara marble
390 (Migliazza et al., 2011). These are the same material properties and initial
391 conditions as in Delbo et al. (2014). To the best of our knowledge, the only
392 thermal fatigue experiments that have been conducted on meteorite samples
393 are those conducted by Delbo et al. (2014) and Hazeli et al. (2018). The
394 observed crack growth in the experiments of Delbo et al. (2014) is well repre-
395 sented by a thermo-mechanical model similar to the one described here and
396 a crack growth rate following the Paris law with parameters values similar to
397 those of Carrara marble (from Migliazza et al. (2011)). Delbo et al. (2014)
398 performed also an uncertainty analysis and showed that values different than
399 more than 30% from those of Carrara marble would not explain the labora-
400 tory experiment data on meteorites. The stress intensity factor is recorded
401 at time increments of 15 minutes. At the end of a complete cycle, the ex-
402 cursion between the maximum and the minimum stress intensity factor is
403 determined and the equivalent stress intensity factor excursion is calculated
404 using Eq. (13). Then, Eqs. (12) and (14) are used to calculate the crack
405 length increment and direction.

Table 1: Values and base dimensions assumed for the physical properties of the carbonaceous chondrite material considered in this study. The base dimensions are expressed in the $MLT\theta$ (Mass-Length-Time-Temperature) system.

	Symbol	Units	Dimensions	Carbonaceous Chondrite	Ordinary Chondrite	Reference
Paris exponent	n	-	-	3.84	3.84	Migliazza et al. (2011)
Paris pre-factor	C	m (MPa \sqrt{m}) $^{-n}$	$L^{1+n/2} M^{-n} T^{2n}$	3×10^{-4}	3×10^{-4}	Migliazza et al. (2011)
Young's Modulus	E	GPa	$M L^{-1} T^{-2}$	45	74	Delbo et al. (2014)
Poisson's ratio	ν	-	-	0.24	0.28	Delbo et al. (2014)
Bulk expansion coefficient	α_m	K^{-1}	θ^{-1}	8.5×10^{-6}	8.5×10^{-6}	Hazen (1977)
Chondrule expansion coefficient	α_{mc}	K^{-1}	θ^{-1}	10.4×10^{-6}	10.4×10^{-6}	Smyth (1975)
Thermal Conductivity	κ	$W m^{-1} K^{-1}$	$M L T^{-3} \theta^{-1}$	0.5	1.88	Opeil et al. (2010)
Specific Heat Capacity	C_p	$J kg^{-1} K^{-1}$	$L^2 T^{-2} \theta^{-1}$	500	550	Opeil et al. (2010)
Bulk density	ρ	$kg m^{-3}$	$M L^{-3}$	1662	3150	Opeil et al. (2010)
Thermal inertia	Γ	$J m^{-2} s^{-0.5} K^{-1}$	$M T^{-5/2} \theta^{-1}$	640	1800	Opeil et al. (2010)
Rotation period	τ	h	T	6	6	-

406 Although our modeling approach is able to solve for arbitrarily growing
407 cracks, recall that the temperature field computed from the thermal model
408 is one-dimensional (that is, the temperature at a given time is a function
409 of only one direction) and that the geometry and crack configuration are
410 symmetric. This symmetry in geometry and loading implies that no mode-II
411 fragmentation will occur ($\Delta K_{II} = 0$ in every cycle), and consequently the
412 crack will propagate over a straight path without any kinking ($\theta = 0$). Given
413 these idealizations, we consider the rock to be broken when the initial surface
414 crack length becomes nearly equal to the rock diameter; that is, when the
415 crack extends to the bottom-most element in the mesh. Note that a break
416 in symmetry could occur when using a 2-D temperature field, or including
417 multiple initial cracks, or an initially inclined surface crack. In these cases,
418 fragments could also be produced by the coalescence of multiple cracks or by
419 flaking surface material. While such scenarios can be captured reasonably
420 through our numerical model, they are not considered in this work in the
421 interest of first extracting some key physical ideas that can be simply applied
422 for different asteroids in the solar system.

423 We have performed thermal fatigue simulations for such carbonaceous

424 chondrites of diameters between 1 cm and 50 cm, and our results on the
425 thermal fragmentation of these rocks are presented in Fig. 5. The figure
426 shows the time taken (in years) to fragment a rock of a given size (the blue
427 data points are obtained from our simulations). All rocks are assumed to
428 have an initial 30μ m crack. Due to the numerical resolution and the nature
429 of the contour integral, this crack typically grows to around 0.1 of the rock
430 diameter during the first few cycles. As such, we do not expect a large de-
431 viation in the survival times as a result of the initial crack size. The bars
432 around each data point represent a variation of 30% in the Paris coefficient
433 C . Note that the computed survival times can be as high as 10^8 years, while
434 the thermal cycling period is 6 hours, demonstrating the need for an efficient
435 computational scheme to handle this wide range of timescales. For rocks
436 smaller than 7 cm, our model predicts rock survival times (Fig. 5, in blue)
437 that are consistent with those reported in Delbo et al. (2014) (Fig. 5, in
438 red) using lower-accuracy computations. We predict longer fragmentation
439 times than Delbo et al. (2014), but our more accurate results are still within
440 their reported error margins. Our simulations also show that small rocks
441 will take longer to fracture through thermal fatigue than larger rocks (up to
442 approximately 7 cm). The trend captured here and in Delbo et al. (2014)
443 has also been stipulated by Molaro et al. (2017) for lunar rocks (albeit from
444 purely stress-based arguments). However, Fig. 5 shows that beyond approx-
445 imately 7 cm, this trend is reversed, in that larger rocks require increasingly
446 longer times to fragment. This is primarily because although larger thermal
447 gradients may cause larger stresses, the largest temperature fluctuations are
448 limited to the near-surface (Figs. 1 and 4), and temperature changes become

449 negligible far from the skin depth. When cracks reach a size larger than the
450 skin depth, the driving force at the crack tip gradually decreases, and the
451 rate of growth of the crack is slowed down.

452 For comparison, Fig. 5 also shows the survival times of the rocks as a con-
453 sequence of the micrometeorite impact mechanism, as calculated using the
454 results from Hörz et al. (1975), with the modifications applicable to asteroid
455 surfaces made in Delbo et al. (2014). In Delbo et al. (2014), the mechani-
456 cal disruption estimates were calculated for the 99% probability of survival.
457 However, Hörz et al. (1975) notes that the maximum survival times could be
458 up to 25% shorter than this upper bound, depending on the exact particle
459 abrasion rates and the continuously decreasing effective cross-section caused
460 by the abrasion. To provide a more conservative comparison between thermal
461 fatigue and mechanical disruption, we consider here the 50% probability of
462 survival of the rocks by mechanical impacts (dashed line in Fig. 5). **Note that**
463 **observational evidence suggests that the rock breakdown rate on the Moon is**
464 **at least a factor of 5 higher than the Horz model predicts** (Basilevsky et al.,
465 2013). **The model may thus underestimate breakdown rates due to microm-**
466 **eteorite impacts.** Comparison of the thermal fatigue and impact breakdown
467 mechanisms thus shows that the impact process may become at least as effi-
468 cient a breakdown process as thermal fatigue for rocks as large as 50 cm, and
469 is likely to be more efficient than thermal fatigue for larger rocks. Note again
470 that this computation is for **C-type asteroids** at 1 AU and with a diurnal
471 cycle of 6 hours.

472 The driving force for such sub-critical fatigue crack growth is the excu-
473 sion in stress intensity factor ΔK , as shown in the Paris law (Eq. (12)). For

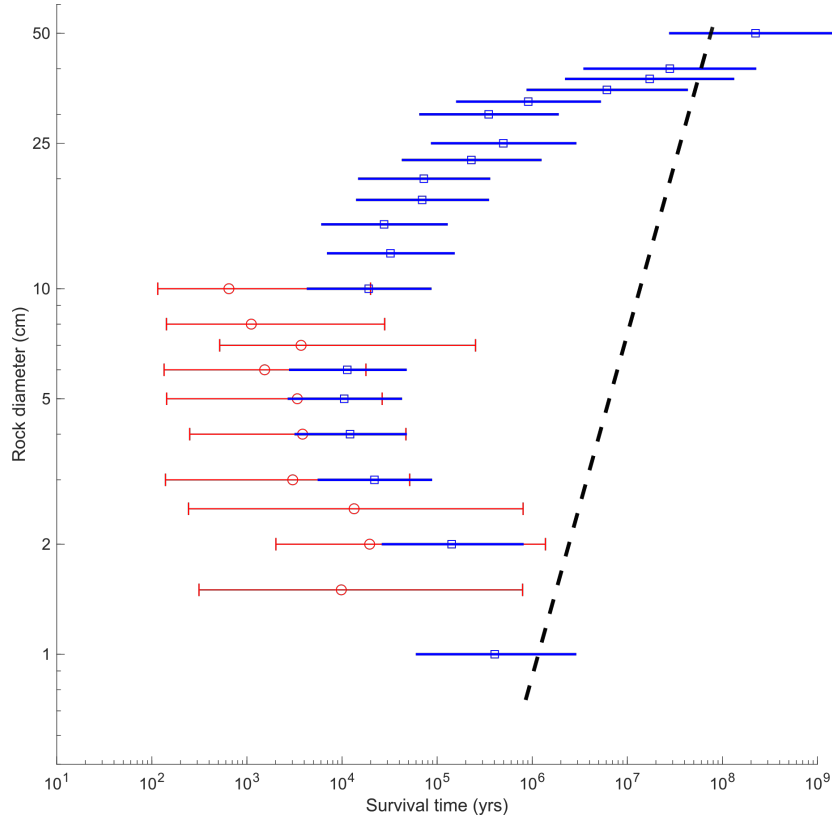


Figure 5: Survival time of cm-sized (diameter) carbonaceous chondrites at 1 AU and a diurnal cycle of 6 hours. The data points in red are from Delbo et al. (2014), while the blue data points are obtained from the model presented in this work. Error bars represent uncertainties (30% variation) in the Paris' parameters. The dashed line shows the times at which 50% of these same rocks are broken by micrometeoroid impacts, using the Hörz et al. (1975) model with the appropriate modifications for asteroids. The survival times of rocks smaller than the diurnal skin depth (approx. 7 cm) follows the same trend as reported in Delbo et al. (2014): larger rocks are fragmented faster than smaller rocks. However, as rock diameters become larger than the skin depth, a reversal in the trend is observed. That is, the crack growth speed of thermal fatigue driven surface crack is greatly reduced in these larger rocks.

474 all crack sizes shown here, the maximum stress intensity factor is always
475 smaller than the fracture toughness K_{IC} , and the crack grows only in fatigue
476 and no dynamic fracture occurs.

477 In order to obtain a better understanding of the non-monotonic effect of
478 thermal fatigue with respect to rock size, Fig. 6 shows the computed excursion
479 in stress intensity factor (normalized by the material's fracture toughness)
480 as a function of crack length (normalized by the rock diameter) for rocks of
481 a range of sizes. Note that when the normalized crack length reaches 1, the
482 rock is completely broken. Looking first at the rocks that are less than 10 cm
483 in diameter, we see that there is an increasing trend in ΔK with increasing
484 crack length. This means that for these rocks, the driving force for crack
485 growth increases as the crack grows (so that for the same thermal cycles, the
486 rock is increasingly likely to break as the initial crack increases in length as
487 a result of prior thermal cycles). Thus the crack growth accelerates as the
488 crack grows. However, this is only true for rocks that are smaller than the
489 diurnal skin depth. For the larger rocks, with diameters > 10 cm in this
490 case, we see from Fig. 6 that the crack tip driving force ΔK decreases as the
491 crack grows, leading to a decrease in the crack growth rate, and thus these
492 larger rocks take an increasingly long time to break. This is true even though
493 these larger rocks do sustain large thermal gradients. The decrease in the
494 driving force is greater for larger rocks in this size domain, and thus larger
495 rocks take a longer time to fragment through thermal fatigue. Essentially
496 our detailed simulations show that for rock sizes significantly larger than
497 the diurnal skin depth, thermal fatigue can efficiently grow cracks up to a
498 certain size (roughly 60% of the diameter), but after that crack growth is

499 greatly slowed down.

500 Note that this observation is largely independent of the chosen crack
501 growth law. The crack tip driving force that we compute here in Fig. 6 de-
502 pends on the current crack length rather than the crack growth history, and
503 so this change in crack tip driving force will be observed regardless of the
504 specific growth law. Here we assume a simple Paris-type relationship for fa-
505 tigue growth, which may not properly describe the crack tip speed in thermal
506 fatigue. Further experimental work is required to determine the applicabil-
507 ity and the parameters of the Paris' law for thermal fatigue crack growth
508 in different meteoritic materials. For a different growth law, the computed
509 crack tip driving force will essentially be the same, but the computed rate of
510 growth of the crack would be different (i.e., how long it takes the crack to
511 cross the rock will change, but the trends with respect to the size effects will
512 be the same).

513 The results of Fig. 6 indicate that there is a characteristic lengthscale that
514 separates two distinct regimes in thermal fatigue: one that is dominated by
515 larger temperature fluctuations happening near the crack tip, and another
516 where the temperature changes become far-field relative to the crack tip
517 location. This characteristic lengthscale is, to first order, determined by the
518 diurnal skin depth (Fig. 1). In addition, the two trends described here and
519 shown in Fig. 5 both appear to follow a power law-type dependence. That
520 is, they may be fit to two distinct slopes on a log-log curve (in the same
521 manner as the mechanical impact scaling). In the next section, we will use
522 the concepts of this lengthscale and size-dependence of the excursion in stress
523 intensity factor to derive a simplified relationship for the survival rate of rocks

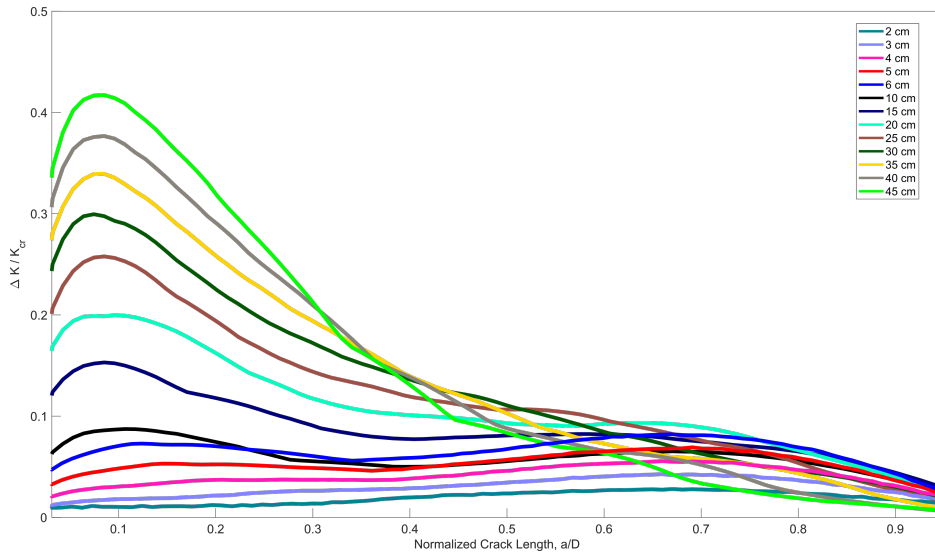


Figure 6: Normalized excursion in stress intensity factor as a function of crack length normalized by the rock diameter. In small (less than 10 cm) rocks, $\Delta K/K_{cr}$ generally increases with increasing crack size, especially between a/d of 0.1 and 0.7. Rocks much larger than the skin depth see a different trend, wherein the excursion in stress intensity factor decreases as the crack size increases. The implications of these trends on the survival rates of asteroid rocks are discussed in Section 3.

524 as a function of rock diameter.

525 3. Scaling Analysis

526 Our fracture mechanics model computes the stress intensity factor excursion
 527 during each asteroid rotation until the fragmentation of the rock. The
 528 **rock's time to fracture** is determined essentially by the number of thermal
 529 cycles that occur before the crack length becomes equal to the rock diameter.
 530 However, the amount of crack growth in a given cycle is not constant,
 531 so that the crack could (for example) spend a very long time (a large number
 532 of cycles) growing very slowly, and then accelerate rapidly and cover the
 533 remaining length in a very few cycles. Thus, in order to obtain a reasonable

534 analytical estimate of the time it takes to crack a given rock, we primarily
535 need to know the conditions under which the crack spends the largest fraction
536 of its time, when it is growing very slowly.

537 Now, the fatigue crack propagation law adopted in this work is the classi-
538 cal Paris law, relating the excursion in stress intensity factor at the crack tip
539 to an incremental displacement of the crack front. In principle, it is therefore
540 sufficient to integrate the Paris law to obtain an estimate for the predicted
541 time to fracture. As Fig. 6 shows, the excursion in the stress intensity factor
542 is itself a fairly nonlinear function of crack length, especially in the largest
543 rocks. However, in terms of estimating the time to fracture, all we need is to
544 know how ΔK depends on crack length during the times when the crack is
545 growing very slowly, since this dominates the total time to fracture.

546 Our simulations show that for “small rocks,” i.e., rocks smaller than the
547 skin depth, ΔK increases approximately linearly with crack length for at
548 least 80% of the total time before fracture (this occurs until the crack length
549 reaches about 70% of the rock’s diameter). The excursion in stress intensity
550 for rocks smaller than the skin depth with normalized crack lengths a/d
551 between 0.1 and 0.7 can be fit to a linear function $\Delta K(a) \approx \bar{A}a + \bar{B}$ with
552 a Pearson correlation coefficient (Lee Rodgers and Nicewander, 1988) $r =$
553 0.988. This linear approximation greatly simplifies the integration of the
554 Paris law, Eq. (12) . In Section 4, we will discuss some of the consequences
555 of this approximation.

556 Now, using the assumption that $\Delta K(a) \approx \bar{A}a + \bar{B}$, with \bar{A} and \bar{B} the
557 linearization parameters, we can integrate the Paris fatigue crack growth law
558 (Eq. (12)) from the initial crack length a_0 at time $t = 0$ to a final crack

559 length $a_f = d$ at the approximated failure time t_f . Now, recognizing that
 560 $dN = 1/\tau dt$ where τ is the period of rotation, we get:

$$\frac{t_f}{\tau} \sim \frac{1}{C\bar{A}(1-n)} \cdot (\bar{A}d + \bar{B})^{1-n} \quad (15)$$

561 Note that here we only seek to understand the power-law dependence
 562 of t_f on d . We do not calculate the exact value of the integral since the
 563 linearization parameters \bar{A} and \bar{B} are different for different rock diameters.
 564 After some analytical simplifications (dropping the \bar{B} terms and setting and
 565 setting $t = t_f$ at $a = d$) to Eq. (15), we can express the time to fracture as a
 566 function of rock diameter as:

$$d \sim \left(\frac{t_f}{\tau}\right)^{\frac{1}{1-n}} [\bar{A}^n C (n-1)]^{\frac{1}{1-n}} \quad (16a)$$

$$\frac{t_f}{\tau} \sim (d)^{1-n} \frac{1}{\bar{A}^n C (n-1)} \quad (16b)$$

567 Eq. (16a) and Eq. (16b) give us relatively simple approximate relationships
 568 between the time to fracture and the size of the rock (for rocks smaller than
 569 the diurnal skin depth), and shows that this relationship is dominated by the
 570 power $\frac{1}{1-n}$ in the former case and $1-n$ in the latter case. Notice that t_f/τ is
 571 dimensionless, and $A^n C$ has base units of L^{1-n} , making the right-hand side
 572 of Eq. (16b) also dimensionless.

573 For the case of rock diameters larger than the diurnal skin depth, the
 574 crack grows quickly to a normalized length of $a/d = 0.2$ in less than 10% of
 575 the total time to fracture. The bulk of the time to fracture occurs as the crack
 576 is growing progressively slower until $a/d \sim 0.95$. For this domain, a linear

577 fit does not capture adequately the shape of the excursion in stress intensity
578 factors, and so the integration cannot be simplified in the same manner as for
579 the smaller rocks. Instead, we directly fit to the final fragmentation times in
580 Fig. 5 and obtain that $d \propto t^{\frac{1}{n-1}}$. We will show that these two slopes provide
581 a good description of the thermal fatigue lifetime of rocks on asteroids with
582 different composition, heliocentric distances, and rotation periods.

583 In order to understand the contributions of the thermophysical and me-
584 chanical variables to the final fragmentation time, we make use of the Buck-
585 ingham π theorem (Buckingham, 1914). The different π -groups are identified
586 by first constructing the dimensional matrix (Brand, 1957) of all variables
587 relevant to the problem (Table 1). Mathematically, the π -groups represent
588 the null-space of the dimensional matrix that are obtained from the matrix's
589 kernel vector. In this analysis, we have the following π -groups:

$$\pi_1 = \frac{d^2 \cdot \rho \cdot C_p}{\kappa \cdot \tau} \quad (17)$$

$$\pi_2 = \frac{d^4 \cdot \rho \cdot \alpha}{\kappa \cdot \tau^3} \quad (18)$$

$$\pi_3 = \frac{\kappa \cdot \tau^3 \cdot \Delta T}{d^4 \cdot \rho} \quad (19)$$

$$\pi_4 = \frac{\tau^2 \cdot E}{d^2 \cdot \rho} \quad (20)$$

$$\pi_5 = \frac{t_f}{\tau} \quad (21)$$

$$(22)$$

590 One must recognize, of course, that this set is not unique as any combination
591 of the dimensionless groups also yields a dimensionless group. However, this

592 particular set has some useful attributes. π_1 is effectively a measure of the
 593 diameter normalized by the skin depth, δ . Eq. (16b) can be re-expressed in
 594 dimensionless form after normalizing the diameters by the skin depth as:

$$\frac{d}{\delta} = \Lambda \left(\frac{t_f}{\tau} \right)^m ; \begin{cases} m = \frac{1}{1-n} & , \quad \frac{d}{\delta} \leq 1 \\ m = \frac{1}{n-1} & , \quad \frac{d}{\delta} > 1 \end{cases} \quad (23)$$

595 where Λ is a scaling parameter related to the number of cycles needed to
 596 fragment a rock with diameter equal to the skin depth. In this form, the
 597 fragmentation time is expressed as a simple a power-law type relation with
 598 the rock diameter and skin depth. The advantage of this scaling relation is
 599 that the survival time of rocks by thermal fatigue can be estimated by per-
 600 forming a single XFEM simulation for a rock of size equal to the skin depth
 601 to determine Λ , and extrapolating to rocks with different sizes using Eq. (23).

602 This scaling analysis thus provides us with a simple way to understand the
 603 effects of thermal fatigue in terms of the time to fracture and rock size.

604 Using this simple scaling, Fig. 7 shows a normalized representation of
 605 Eq. (23) and the survival rates of rocks on small asteroids with the same
 606 rotational period but with different thermomechanical properties (both or-
 607 dinary and carbonaceous chondrites) and heliocentric distances (both near-
 608 Earth asteroids and main-belt asteroids). In addition, we plot a normalized
 609 version of the data presented in Ravaji et al. (2018). Ravaji et al. calcu-
 610 lated the predicted thermal fatigue lifetime of a 10 cm diameter ordinary
 611 chondrite-like rock on a near-Earth asteroid, as a function of the asteroid's
 612 rotation period using the same model of Delbo et al. (2014). They indicate

613 that extrapolation of rock lifetimes for different rotational periods is not lin-
614 ear, but did not indicate how the scaling should be performed. In Fig. 7,
615 we show that by scaling the rock diameter by the skin depth, which itself
616 is a function of rotational period, the survival times of Ravaji et al. (2018)
617 collapse well onto the slopes identified in this work. Despite using a different
618 thermomechanical model, these estimates fit well onto our nondimensional
619 plot, especially for those rocks that are smaller than ~ 4 skin depths. Note
620 that beyond around 5 skin depths, the efficiency of thermal fatigue is greatly
621 reduced, and the scaling arguments overestimate the breakdown rates by an
622 order of magnitude.

623 What remains is to obtain an understanding of the meaning of the scaling
624 parameter Λ . We do this by using a parametric analysis with our simulations
625 to extract the dependence of Λ on C , E , α , and ΔT . This allows us to re-
626 write Eq. (23) as :

$$\frac{d}{\delta} \sim C^{\frac{1}{1-n}} E^{-1.25} \rho^{-0.5} C_p^{-0.5} (\alpha \Delta T)^{-1.5} \left(\frac{t}{\tau} \right)^m \quad (24)$$

627 This is a powerful relationship, because we can now estimate the survival
628 rates of rocks for the same material and similar rotational periods with dif-
629 ferent positions in the solar system (that is, with different ΔT).

630 As an example, by scaling the results from Figs. 5 and 7 using the scaling
631 factors in Eq. (24), we present in Fig. 8 the predicted time to break down
632 (defined by the colored contours) a 10 cm rock on a C-type asteroid as a
633 function of the period of rotation and the heliocentric distance. The dark
634 blue contours are of the order of 10,000 years, and the yellow corresponds to
635 a million years (as shown in the key on the right of the figure). Note that

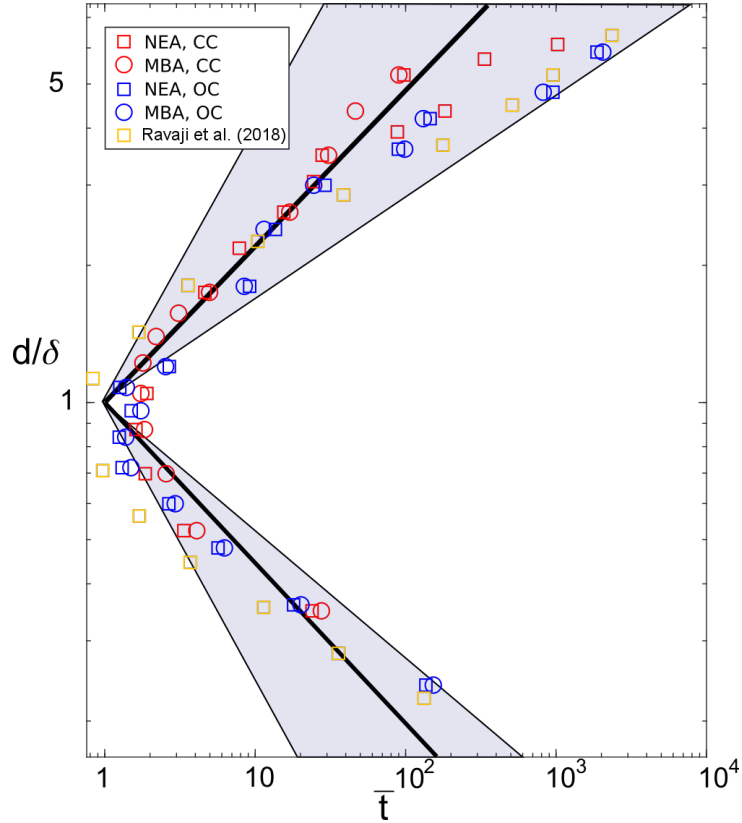


Figure 7: Scaled survival times of carbonaceous chondrites (CC) and ordinary chondrites (OC) on near-Earth asteroids and in the main belt. Circles and squares represent numerical simulation results for main belt and Near-Earth asteroids, respectively. The x -axis is a measure of the survival rates normalized by the number of cycles for fragmenting a rock with diameter equal to the skin depth. It is defined from Eq. (23) as $\bar{t} = (t_f)/t_{\delta f}$, where $t_{\delta f}$ is the fragmentation time for a rock with diameter equal to the skin depth. The y -axis is the rock diameter normalized by the skin depth. With this dimensionless representation, the two slopes intersect at (1,1). The circle and square symbols are results from the numerical model. The solid lines represent the slopes identified in Eq. (16a) and the shaded region represents 30% confidence intervals related to the Paris' exponent n .

636 in Fig. 8, the temperature excursion changes with heliocentric distance, and
637 the skin depth changes with rotation period. We assume a solid, competent
638 bedrock with negligible regolith shielding the temperature excursions. The
639 presence of a layered surface or initial fine-grained regolith blanket would
640 greatly change the estimated skin depth (see discussion in Section 4), and
641 would lead to larger times for disruption. These results therefore are a lower-
642 bound on how fast thermal fatigue could fragment a single rock on the surface
643 of asteroids.

644 The contours in Fig. 8 imply that asteroids at different orbital positions
645 and with different rotational periods may exhibit similar degrees of thermal
646 fatigue on their surfaces. That is, if the thermomechanical properties of rocks
647 on 162173 Ryugu and 101955 Bennu are similar, then they should exhibit
648 similar thermal fatigue breakdown behavior of 10 cm rocks despite having
649 different rotation periods. 162173 Ryugu is being visited by Haybusa2 at
650 the time of this writing (March 2019), and 101955 Bennu is the target of the
651 OSIRIS-REx mission, which began detailed observations of the asteroid at
652 the end of 2018. We hope that our results will therefore help in interpreting
653 the observations from sample characterization for both missions.

654 We also note the existence of an intermediate range in rotational periods
655 (4 – 15 h) where our model predicts that thermal fatigue would be most
656 efficient. Very fast rotators have small skin depths, and larger rocks would
657 require increasingly larger times to fragment. Slow rotators have larger skin
658 depths and rocks much smaller than that skin depth would also take increas-
659 ingly longer times to fragment (see discussion for Fig. 5), as well as requiring
660 a longer time to complete a single period.

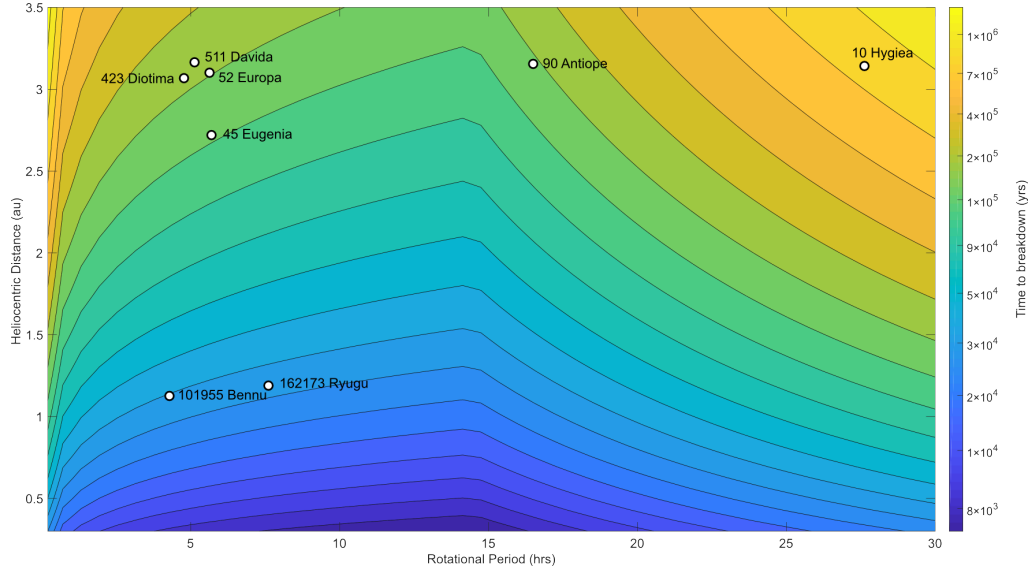


Figure 8: Predicted time (in years) to break down a 10 cm diameter rock on a C-type asteroid as a function of period of rotation and heliocentric distance, using the scaling factors in Eq. (24). Some C-type asteroids are highlighted on the plot using their semi-major axis and rotation period as reference. These were not modeled directly, and discrepancies from Table 1 in their particular surface and material composition would lead to different breakdown rates than those predicted in this figure. These results indicate the existence of an “intermediate” range in rotational periods where thermal fatigue would be more efficient. Very fast rotators have small skin depths, and larger rocks would require increasingly larger times to fragment. Slow rotators have larger skin depths and take longer time to complete a single period, and rocks much smaller than that skin depth would also take increasingly longer times to fragment (see discussion for Fig. 5). **Consequently, the fragmentation times and the ideal “intermediate range” in rotation period depend on the particular rock diameter and how it compares with the skin depth.**

661 4. Discussion

662 For cm-sized rocks, we predict that thermal fatigue can be several orders
663 of magnitude faster than micrometeorite impacts in fragmenting such small
664 rocks on small airless bodies with a ~ 6 h period of rotation, in-line with
665 the results of Delbo et al. (2014). In Delbo et al. (2014), thermal fatigue
666 appeared to occur faster in larger rocks, owing to the larger temperature
667 gradients they experience. Their results for ≤ 10 cm rocks indicated a speed-
668 up of thermal fatigue as rock sizes increase, implying that much larger rocks
669 should be relatively scarce on the surface of asteroids. Similarly, Molaro et al.
670 (2017) reported an increase in peak stresses for large boulders (≥ 1 m) on
671 the lunar surface as opposed to ≤ 30 cm rocks. They concluded, using purely
672 stress-based arguments, that this could suggest a lack of very large boulders
673 (diameters of several skin depths) on airless bodies. However, we have shown
674 here that thermal fatigue is characterized by a signature lengthscale related
675 to the thermal skin depth of the asteroid. While peak stresses due to thermal
676 gradients can increase in larger rocks, they are mostly limited to the near-
677 surface and can be efficiently relaxed with the introduction of a crack. Peak
678 stresses derived from purely elastic solutions are therefore poor indicators
679 of the fatigue behavior. As cracks grow to lengths much larger than the
680 skin depth, the driving force is greatly reduced, leading to a slow-down in
681 thermal fatigue crack advance. Hence, our results imply the existence of a
682 size domain over which thermal fatigue is mostly active.

683 These newfound size domain for thermal fatigue could help in determin-
684 ing the abundance and distribution of cm-sized rocks, which will be the main
685 excavation targets in asteroid mining and sampling missions. For instance,

686 it has been shown that asteroid (433) Eros has a complex regolith (Veverka
687 et al., 2001b,a) whose size-frequency distributions (Thomas et al., 2001) sug-
688 gested that the mechanisms for depleting 20 cm diameter rocks seemed to be
689 very different than those for 100 m blocks. Their observation is in-line with
690 the lengthscales determined in this study, which may imply that thermal
691 fatigue could be a contributing mechanism for the disaggregation of these
692 relatively small surface rocks. In addition, the recently launched OSIRIS-
693 REx mission that is targeting the asteroid (101955) Bennu (Lauretta et al.,
694 2017) will attempt to sample and return a minimum of 60 g from the aster-
695 oid’s bulk regolith. Bennu is a carbonaceous asteroid with a 4.3 h rotation
696 period and an estimated thermal skin depth of ~ 5 cm. In this work, we pre-
697 dict that for such a case, most cm-sized rocks should have experienced some
698 degree of thermal fatigue, and we expect that the sampled rocks returned by
699 OSIRIS-REx should show evidence of an active thermal fatigue mechanism.

700 During the preliminary survey of Bennu, in December 2018, OSIRIS-REx
701 returned images covering 80% of the asteroid surface with a spatial resolu-
702 tion of 33 cm/px, visible, near and thermal infrared spectra (Lauretta et al.,
703 2019). Images show a geomorphologically diverse surface with craters (likely due
704 to impacts) and covered with boulders of sizes ranging from 58 m of length
705 down to the spatial resolution limit (Della Giustina et al., 2019; Walsh et al.,
706 2019). Some of the boulders present evidence of fractures (Walsh et al., 2019),
707 while other boulder arrangement suggest that these are breaking in place
708 (Lauretta et al., 2019). Thermal fatigue is a potential explanation for the ob-
709 served features. Another explanation is thermal dehydration or desiccation
710 of Bennu’s boulders, or a combination of the two. OSIRIS-REx near-infrared

711 spectra clearly indicate the presence of a 20–25% deep absorption band at
712 $2.72\mu\text{m}$, that is typical of hydrated meteorites of type CI or CM (Hamilton
713 et al., 2019). As such, it is possible that dehydration of this material could
714 be responsible for the presence of fractures on boulders. The cumulative size
715 distribution of Bennu’s boulders larger than 8 m (which is the completeness
716 limit) is well represented by a power law with index 2.9 ± 0.3 . On the other
717 hand, asteroid (25143) Itokawa has a value of 3.5 ± 0.1 for the exponent
718 of the power law that best fits its cumulative size distribution of boulders
719 ≥ 10 m (Mazrouei et al., 2014). The area number density of large boulders
720 (≥ 20 m) on Bennu and Itokawa is comparable (Della Giustina et al. (2019)
721 and references therein). This implies that more surface of Itokawa is covered
722 in small particles than is the case for Bennu. In addition, OSIRIS-REx imag-
723 ing data from Bennu’s preliminary survey rule out a surface covered with
724 centimeter or decimeter sized particles, but are consistent with the possible
725 presence of much finer particles (Della Giustina et al., 2019). In summary,
726 OSIRIS-REx preliminary survey results supports fracturing process at the
727 surface of Bennu and the scarcity of centimeter or decimeter sized particles,
728 consistent with theoretical prediction from this work. At the beginning of
729 March 2019, OSIRIS-REx will commence its detailed survey of Bennu, dur-
730 ing which a global coverage of the surface at the spatial resolution of few
731 centimeters will be obtained. The detailed survey data will enable a better
732 understanding of the smaller rocks on Bennu to be obtained.

733 Furthermore, the effects of thermal fatigue could possibly be identifiable
734 in the thermal inertia measurements. It has been shown that the thermal
735 inertia of surfaces covered with small particles (sand-like regolith) is smaller

736 than those covered by rocky fragments (of ~ 10 cm diameter) (Golombek
737 and Rapp, 1997). In that sense, a small fast-rotating asteroid with a large
738 surface temperature variation would generate an increased number of small
739 fragments, which could lead to a decrease in the measured thermal inertia.
740 Therefore, in the cases where thermal fatigue is driving the regolith evolution,
741 thermal inertia (and skin depth) could be direct indicators of the evolution
742 history of the rock sizes that blanket an asteroid’s surface. Further research
743 is needed to explore the possible relationship, if any, between thermal inertia
744 and thermal fatigue.

745 For sufficiently large rocks, our model suggests that thermal fatigue would
746 be more efficient in flaking off material from the surfaces as opposed to a com-
747 plete fracture, which results in an apron of small (cm-sized) rocks surrounding
748 larger boulders. This behavior has been observed on (433) Eros (Robinson
749 et al., 2001), where the aprons provided evidence that boulders are eroding
750 in place, giving a probable explanation for the nearly 300 pond-like features
751 on Eros (Dombard et al., 2010). Such cases may be investigated through our
752 model by solving for the $2D$ temperature field and tracking the growth of
753 multiple crack networks in the thermomechanical XFEM model. The results
754 derived here rely on a $1D$ thermal solution of an idealized spherical asteroid.
755 The temperature profile does not treat surface roughness, shadowing effects,
756 or changes in thermal conduction introduced by cracks or rock boundaries.
757 A more sophisticated thermal model may lead to a different temperature
758 profile than that in Fig. 1, which would give a different crack tip driving
759 force (Fig. 6). As an additional caveat, an estimation of thermal fatigue in
760 particular rocks with local shadowing may not be a straight-forward extrap-

761 olation of our results and would require using the numerical model with the
762 appropriate temperature inputs.

763 While our new thermomechanical model constitutes a significant advance
764 from previous semi-analytical models, it is still important to realize the sim-
765 plifications and inherent assumptions that we have made. For instance, we
766 are now using a two-dimensional mechanical model with thermal inputs from
767 a one-dimensional heat diffusion model. We do not consider the cases where a
768 crack deviates from a straight path, which may cause scabbing of the larger
769 rocks by gradually chipping off material from the surface. A break of the
770 symmetry could occur when using a 2D temperature field, or with the inter-
771 action of multiple initial cracks. In these cases, fragments could be produced
772 by crack coalescence or by flaking surface material. Given that an idealized
773 case of a single thermal fatigue crack growth model has demonstrated the im-
774 portance of this mechanism, it is worthwhile to make future efforts to include
775 the more complex behavior of a network of cracks, as well as the coupling
776 between thermal fatigue and mechanical impact. It is unlikely that rocks on
777 airless bodies would have only a single active surface crack that drives the
778 thermal fragmentation.

779 Natural geological materials have a large distribution of flaws with dif-
780 ferent sizes and orientations. These flaws can evolve by thermal fatigue, but
781 are also modified through non-catastrophic micrometeoritic impacts. Im-
782 pacts by micrometeorites nucleate and propagate cracks, which can then be
783 grown through fatigue. In that sense, these two mechanisms are collabo-
784 rating processes in asteroidal regolith generation: micro-meteoritic impacts
785 nucleate cracks in rocks that will propagate due to thermal fatigue, which in

786 turn weakens the body making a subsequent impact more effective.

787 The numerical model developed in this work has the capability to cal-
788 culate the crack-tip driving forces resulting from the interaction of a large
789 network of cracks. However, it is unclear if the Paris law would still be
790 an appropriate representation of the crack growth rates. The Paris law pa-
791 rameters are empirical fits to fatigue experiments on single crack growth.
792 In addition, uncertainty quantification through surrogate modeling of fa-
793 tigue growth (Sankararaman et al., 2011) showed a major contribution of the
794 Paris' C parameter to the errors in predicted fatigue cycles. These parame-
795 ter uncertainties contribute to large error bars in the fatigue life prediction.
796 Atkinson (1984) demonstrated that different forms of the Paris law could
797 yield essentially identical predicted growth rates for laboratory-scale experi-
798 ments. In geophysical applications, however, we need to extrapolate beyond
799 the bounds of laboratory scales, and different forms of the Paris law diverge
800 substantially, with the form chosen in this work yielding the most conserva-
801 tive estimates. In our simulations, the crack always grew in fatigue mode.
802 There may be a limit for how small the excursion in stress intensity factors
803 should be for any growth to occur (typically known as the stress intensity
804 threshold). So far, there has not been any clear experimental evidence of the
805 existence of a subcritical crack growth limit or threshold for crack growth
806 in geological material. Indeed, fatigue experiments performed by Wilkins
807 (1980) on granite showed crack speeds as low as 10^{-11} – 10^{-12} m/s without
808 encountering a crack arrest limit. The reliable prediction of thermal fatigue
809 lifetime of rocks is therefore limited by the absence of a significant database
810 fatigue experiments on planetary materials and in environments comparable

811 to airless bodies (for example, thermal cycling experiments conducted in a
812 vacuum chamber). Regardless of the exact growth law being used (assuming
813 cracks are growing sub-critically in fatigue), we do not expect that the size-
814 dependence we identify in this work to be affected. The crack tip driving
815 forces (shown in Fig. 6) are insensitive to the precise expression of the crack
816 growth law. The *rate* of breakdown as a function of rock diameter, however,
817 would be greatly affected.

818 We note that several stress relaxation mechanisms such as creep could
819 occur during these long loading cycles that may modify the stress response
820 and crack growth behavior. These relaxation effects have been reported in
821 sedimentary and hard rocks (Maranini and Brignoli, 1999; Fujii et al., 1999; Li
822 and Xia, 2000), and can relax peak stresses by 10–15% in roughly 13 hours.
823 It is not inconceivable, then, that microstructure evolution through creep
824 would relax the induced diurnal thermal stresses over the course of several
825 thousands of years, leading to a slower thermal fatigue cracking.

826 Mismatches in expansion coefficients between the individual grains could
827 play an important role in driving the thermal fatigue fragmentation of re-
828 golith with sizes much smaller than the skin depth. In this work, we consider
829 an averaged contribution to the stress tensor from inclusions by means of a
830 sub-scale representative volume element approach. With this homogeniza-
831 tion approach, it is possible that the stresses arising from thermal mismatch
832 alone could be underrepresented, especially in the smaller rocks.

833 The simplified analytical integration of the Paris law presented in Sec-
834 tion 3 showed a good fit to the numerical model results despite using a linear
835 approximation of the excursion stress intensity factors. The derived analyti-

836 cal expressions for the breakdown time can therefore be used for a first-order
837 estimate of thermal fatigue fragmentation for rocks that are of the same order
838 as the skin depth. Rocks with diameters that were much larger than the skin
839 depth showed weak response to thermal cycling, suggesting that the thermal
840 fatigue response would be very weak beyond such sizes. We note also that
841 thermal fatigue scaling is highly nonlinear with changes in rotation period.
842 This is in a small part due to the longer times associated with each fatigue
843 cycle, but is more dependent on the resulting surface temperature variations
844 and its spatiotemporal evolution. Fast rotators (periods of 2-4 hours) expe-
845 rience more thermal cycles for the same amount of time as slower rotators
846 (periods of 12 hours or more). However, a fast rotator experiences smaller
847 temperature variations per cycle, and therefore smaller driving forces on the
848 crack. This suggests that thermal fatigue would be most efficient on “inter-
849 mediate” rotators (periods of rotation ~ 6 hours), and the scaling arguments
850 developed in this work would be best applied to such asteroids. In addition,
851 a layered subsurface in asteroids would greatly affect the temperature profile
852 (and gradients) from that shown in Fig. 1. Mellon et al. (2004) showed that
853 the magnitude of temperature oscillation can be reduced in the subsurface by
854 a factor of 5 in a layered subsurface. Similarly, Molaro et al. (2017) showed
855 that the regolith provides a strong insulation to buried rocks on the lunar
856 surface and reduces their temperature excursion by a factor of almost 18. For
857 these cases, which in our study would be analogous to a reduction in both
858 the skin depth and the temperature excursion, we would not expect to see
859 significant thermal fatigue crack growth in those buried rocks.

860 Modeling thermal fatigue is a computationally intensive process that re-

861 quires careful tracking of the crack front over a large number of cycles. The
862 computational framework needs to be able to bridge efficiently between the
863 relatively fast rotational periods (several hours), to the final fragmentation
864 time of a rock (thousands to millions of years). The numerical model pre-
865 sented here is designed to efficiently model the fatigue growth of cracks in
866 **regolith** over a several thousands of years, while using timesteps as small as
867 15 minutes. More sophisticated fracture codes, such as the mapped finite
868 element method (Chiaramonte et al., 2017), have been developed recently.
869 The mapped finite element method provides a high-order approximation of
870 problems with cracks and yields optimal convergence rates without additional
871 degrees of freedom or special shape functions. Such models may provide im-
872 proved accuracy at reduced computational costs and their implementation
873 in the code developed in this work could be potential paths for improving
874 the numerical algorithm. This advance in numerical modeling capabilities
875 further emphasizes the need for careful baseline thermal fatigue experiments
876 that constrain the material parameters and crack growth laws that are used
877 in such predictive models.

878 **5. Conclusions**

879 We find that the rate of rock breakdown by thermal fatigue has two
880 domains that are described by distinct slopes (Fig. 5). Using an approximate
881 integration of the Paris law based on the results of the detailed fracture
882 simulations, we derive measures for these two slopes. Normalized plots of
883 computed fragmentation times for different rock diameters seem to align
884 well under these analytically derived curves. Our analysis demonstrates that

885 rocks with diameters much larger than the diurnal skin depth will exhibit
886 poor thermal fatigue cracking. In such rocks, cracks can grow quickly by
887 thermal fatigue up to a certain length, after which their progress is slowed
888 down greatly (or even arrested completely).

889 The identification of this critical lengthscale provides bounds on the ar-
890 eas where thermal fatigue is likely to be the dominant mechanism in rock
891 disaggregation. We expect that large boulders would not be fragmented
892 completely by thermal fatigue, but would have long straight cracks that
893 grow in the direction of maximum circumferential thermal stress, just as
894 in the Martian boulders shown in Eppes et al. (2015). We expect that this
895 critical lengthscale may be an important indicator for the expected regolith
896 size distribution. The thermal fatigue contribution may thus be reflected as
897 deviations in the regolith particle size-frequency distribution as a result of
898 preferentially depleting rocks that are of dimensions comparable to the skin
899 depth.

900 **6. Acknowledgements**

901 This work was supported by the Solar System Exploration Research
902 Virtual Institute (SSERVI) and the Hopkins Extreme Materials Institute
903 (HEMI). The numerical simulations were performed on the Maryland Ad-
904 vanced Research Computing Center (MARCC) cluster. MD acknowledges
905 support from the Centre National d’Etudes Spatiales, as well as the Academies
906 of Excellence on Complex Systems and Space, Environment, Risk and Re-
907 siliance of the Initiative d’EXcellence “Joint, Excellent, and Dynamic Initia-
908 tive” (IDEX JEDI) of the Université Côte d’Azur.

909 **References**

- 910 Ajaja, J., Barthelat, F., 2016. Damage accumulation in a carbon fiber fabric
911 reinforced cyanate ester composite subjected to mechanical loading and
912 thermal cycling. *Composites Part B: Engineering* 90, 523–529. doi:10.
913 1016/j.compositesb.2015.09.054.
- 914 Alarcon, E., Brebbia, C., Dominguez, J., 1978. The boundary element
915 method in elasticity. *International Journal of Mechanical Sciences* 20, 625–
916 639. doi:10.1016/0020-7403(78)90021-8.
- 917 Anderson, T.L., 2017. *Fracture mechanics: fundamentals and applications*.
918 CRC Press.
- 919 Atkinson, B.K., 1984. Subcritical crack growth in geological materials. *Jour-*
920 *nal of Geophysical Research: Solid Earth* 89, 4077–4114. doi:10.1029/
921 JB089iB06p04077.
- 922 Barsoum, R.S., 1976. On the use of isoparametric finite elements in lin-
- 923 ear fracture mechanics. *International Journal for Numerical Methods in*
924 *Engineering* 10, 25–37. doi:10.1002/nme.1620100103.
- 925 Basilevsky, A., Head, J., Horz, F., 2013. Survival times of meter-sized boul-
- 926 ders on the surface of the moon. *Planetary and Space Science* 89, 118–126.
- 927 Bathe, K.J., 2014. *Finite element procedures*. 2 ed., Prentice-Hall, Engle-
- 928 wood Cliffs, N.J.
- 929 Belytschko, T., Black, T., 1999. Elastic crack growth in finite elements
930 with minimal remeshing. *International Journal for Numerical Methods in*

- 931 Engineering 45, 601–620. doi:10.1002/(SICI)1097-0207(19990620)45:
932 5<601::AID-NME598>3.0.CO;2-S.
- 933 Benzley, S.E., 1974. Representation of singularities with isoparametric finite
934 elements. International Journal for Numerical Methods in Engineering 8,
935 537–545. doi:10.1002/nme.1620080310.
- 936 Biernacki, K., Szyszkowski, W., Yannacopoulos, S., 1999. Experimental
937 study of large scale model composite materials under thermal fatigue.
938 Composites Part A: Applied Science and Manufacturing 30, 1027–1034.
939 doi:10.1016/S1359-835X(99)00014-7.
- 940 Blackburn, W., 1973. Calculation of Stress Intensity Factors at Crack
941 Tips Using Special Finite Elements, in: The Mathematics of Fi-
942 nite Elements and Applications. Elsevier, pp. 327–336. doi:10.1016/
943 B978-0-12-747250-8.50023-0.
- 944 Bordas, S., Nguyen, P.V., Dunant, C., Guidoum, A., Nguyen-Dang, H.,
945 2007. An extended finite element library. International Journal for Nu-
946 merical Methods in Engineering 71, 703–732. doi:10.1002/nme.1966,
947 arXiv:1010.1724.
- 948 Bowie, O., Neal, D., 1970. A modified mapping-collocation technique for
949 accurate calculation of stress intensity factors. International Journal of
950 Fracture Mechanics 6. doi:10.1007/BF00189828.
- 951 Brand, L., 1957. The Pi theorem of dimensional analysis. Archive for Ratio-
952 nal Mechanics and Analysis 1, 35–45. doi:10.1007/BF00297994.

- 953 Buckingham, E., 1914. On physically similar systems; Illustrations of the
954 use of dimensional equations. *Physical Review* 4, 345–376. doi:10.1103/
955 PhysRev.4.345, arXiv:arXiv:1011.1669v3.
- 956 Chan, S., Tuba, I., Wilson, W., 1970. On the finite element method in linear
957 fracture mechanics. *Engineering Fracture Mechanics* 2, 1–17. doi:10.1016/
958 0013-7944(70)90026-3.
- 959 Chiaramonte, M.M., Shen, Y., Lew, A.J., 2017. Mapped finite element meth-
960 ods: High-order approximations of problems on domains with cracks and
961 corners. *International Journal for Numerical Methods in Engineering* 111,
962 864–900. doi:10.1002/nme.5486.
- 963 Cruse, T.A., 1988. *Boundary Element Analysis in Computational Frac-*
964 *ture Mechanics*. volume 1. Springer Netherlands. doi:10.1007/
965 978-94-009-1385-1.
- 966 Daux, C., Moës, N., Dolbow, J., Sukumar, N., Belytschko, T., 2000. Ar-
967 bitrary branched and intersecting cracks with the extended finite ele-
968 ment method. *International Journal for Numerical Methods in Engi-*
969 *neering* 48, 1741–1760. doi:10.1002/1097-0207(20000830)48:12<1741::
970 AID-NME956>3.0.CO;2-L.
- 971 Davidsson, B.J., Rickman, H., Bandfield, J.L., Groussin, O., Gutiérrez, P.J.,
972 Wilska, M., Capria, M.T., Emery, J.P., Helbert, J., Jorda, L., Maturilli,
973 A., Mueller, T.G., 2015. Interpretation of thermal emission. I. The effect
974 of roughness for spatially resolved atmosphereless bodies. *Icarus* 252, 1–21.
975 doi:10.1016/j.icarus.2014.12.029.

- 976 Delbo, M., Libourel, G., Wilkerson, J., Murdoch, N., Michel, P., Ramesh,
977 K.T., Ganino, C., Verati, C., Marchi, S., 2014. Thermal fatigue as the
978 origin of regolith on small asteroids. *Nature* 508, 233–236. doi:10.1038/
979 nature13153.
- 980 Delbo, M., Mueller, M., Emery, J.P., Rozitis, B., Capria, M.T., 2015. As-
981 teroid Thermophysical Modeling, in: *Asteroids IV*. University of Arizona
982 Press. doi:10.2458/azu_uapress_9780816532131-ch006.
- 983 Della Giustina, D.N., Emery, J.P., Golish, D.R., Rozitis, B., 2019. The
984 regolith of (101955) bennu from osiris-rex imaging and thermal analysis.
985 in press, *Nature Astronomy* .
- 986 Dombard, A.J., Barnouin, O.S., Prockter, L.M., Thomas, P.C., 2010.
987 Boulders and ponds on the Asteroid 433 Eros. *Icarus* 210, 713–721.
988 doi:10.1016/j.icarus.2010.07.006.
- 989 El-Maarry, M.R., Thomas, N., Gracia-Berná, A., Marschall, R., Auger, A.T.,
990 Groussin, O., Mottola, S., Pajola, M., Massironi, M., Marchi, S., Höfner,
991 S., Preusker, F., Scholten, F., Jorda, L., Kührt, E., Keller, H.U., Sierks, H.,
992 A’Hearn, M.F., Barbieri, C., Barucci, M.A., Bertaux, J.L., Bertini, I., Cre-
993 monese, G., Da Deppo, V., Davidsson, B., Debei, S., De Cecco, M., Deller,
994 J., Güttler, C., Fornasier, S., Fulle, M., Gutierrez, P.J., Hofmann, M.,
995 Hviid, S.F., Ip, W.H., Knollenberg, J., Koschny, D., Kovacs, G., Kramm,
996 J.R., Küppers, M., Lamy, P.L., Lara, L.M., Lazzarin, M., Lopez Moreno,
997 J.J., Marzari, F., Michalik, H., Naletto, G., Oklay, N., Pommerol, A.,
998 Rickman, H., Rodrigo, R., Tubiana, C., Vincent, J.B., 2015. Fractures on

- 999 comet 67P/Churyumov-Gerasimenko observed by Rosetta/OSIRIS. Geo-
1000 physical Research Letters 42, 5170–5178. doi:10.1002/2015GL064500.
- 1001 Eppes, M.C., Willis, A., Molaro, J., Abernathy, S., Zhou, B., 2015. Cracks
1002 in Martian boulders exhibit preferred orientations that point to solar-
1003 induced thermal stress. Nature Communications 6, 6712. doi:10.1038/
1004 ncomms7712.
- 1005 Erdogan, F., Sih, G.C., 1963. On the Crack Extension in Plates Under
1006 Plane Loading and Transverse Shear. Journal of Basic Engineering 85,
1007 519. doi:10.1115/1.3656897.
- 1008 Evans, A.G., 1974. The role of inclusions in the fracture of ceramic materi-
1009 als. Journal of Materials Science 9, 1145–1152. doi:10.1007/BF00552831,
1010 arXiv:arXiv:1011.1669v3.
- 1011 Fujii, Y., Kiyama, T., Ishijima, Y., Kodama, J., 1999. Circumferential
1012 strain behavior during creep tests of brittle rocks. International Jour-
1013 nal of Rock Mechanics and Mining Sciences 36, 323–337. doi:10.1016/
1014 S0148-9062(99)00024-8.
- 1015 Gault, E.D., Horz, F., Brownlee, E., Hartung, B.J., 1974. Mixing of the lunar
1016 regolith, in: Proceedings of the Fifth Lunar Conference, pp. 2365–2386.
- 1017 Glinka, G., Shen, G., 1991. Universal features of weight functions for cracks
1018 in mode I. Engineering Fracture Mechanics 40, 1135–1146. doi:10.1016/
1019 0013-7944(91)90177-3.
- 1020 Golombek, M., Rapp, D., 1997. Size-frequency distributions of rocks on Mars

- 1021 and Earth analog sites: Implications for future landed missions. *Journal*
1022 *of Geophysical Research* 102, 4117. doi:10.1029/96JE03319.
- 1023 Gregersen, E., 2009. *The Outer Solar System: Jupiter, Saturn, Uranus, Nep-*
1024 *tune, and the Dwarf Planets.* Britannica Educational Pub. in association
1025 with Rosen Educational Services, New York, NY.
- 1026 Hamilton, V.E., Simon, A.A., Christensen, P.R., C., R.D., 2019. Evidence
1027 for widespread hydrated minerals on asteroid (101955) bennu. in press,
1028 *Nature Astronomy* .
- 1029 Hazeli, K., Mir, C.E., Papanikolaou, S., Delbo, M., Ramesh, K., 2018. The
1030 origins of asteroidal rock disaggregation: Interplay of thermal fatigue and
1031 microstructure. *Icarus* 304, 172–182. doi:10.1016/j.icarus.2017.12.
1032 035.
- 1033 Hazen, R.M., 1977. Temperature, pressure and composition: Structurally
1034 analogous variables. *Physics and Chemistry of Minerals* 1, 83–94. doi:10.
1035 1007/BF00307981.
- 1036 Henshell, R.D., Shaw, K.G., 1975. Crack tip finite elements are unnecessary.
1037 *International Journal for Numerical Methods in Engineering* 9, 495–507.
1038 doi:10.1002/nme.1620090302.
- 1039 Hörz, F., Schneider, E., Gault, D.E., Hartung, J.B., Brownlee, D.E., 1975.
1040 Catastrophic rupture of lunar rocks: A Monte Carlo simulation. *The Moon*
1041 13, 235–258. doi:10.1007/BF00567517.
- 1042 Housen, K.R., Wilkening, L.L., 1982. Regoliths on small bodies in the solar

1043 system. *Annual Review of Earth and Planetary Sciences* 10, 355–376.
1044 doi:10.1146/annurev. ea.10.050182.002035.

1045 Housen, K.R., Wilkening, L.L., Chapman, C.R., Greenberg, R., 1979. Aster-
1046 oidal regoliths. *Icarus* 39, 317–351. doi:10.1016/0019-1035(79)90145-3.

1047 Hsueh, C.H., Becher, P.F., 1996. Residual thermal stresses in ceramic com-
1048 posites. Part I: With ellipsoidal inclusions. *Materials Science and Engi-
1049 neering A* 212, 22–28. doi:10.1016/0921-5093(96)10176-3.

1050 Karihaloo, B.L., Xiao, Q.Z., 2003. Modelling of stationary and growing cracks
1051 in FE framework without remeshing: A state-of-the-art review. *Computers
1052 and Structures* 81, 119–129. doi:10.1016/S0045-7949(02)00431-5.

1053 KC, A., Kim, J.H., 2008. Interaction integrals for thermal fracture of func-
1054 tionally graded materials. *Engineering Fracture Mechanics* 75, 2542–2565.
1055 doi:10.1016/j.engfracmech.2007.07.011.

1056 Lauretta, D.S., Balram-Knutson, S.S., Beshore, E., Boynton, W.V., et al.,
1057 2017. OSIRIS-REx: Sample Return from Asteroid (101955) Bennu. *Space
1058 Science Reviews* 212, 925–984. doi:10.1007/s11214-017-0405-1.

1059 Lauretta, D.S., Della Giustina, D.N., Bennet, C.A., Golish, D.R., 2019. The
1060 unexpected surface of asteroid (101955) bennu. in press, *Nature* .

1061 Lee Rodgers, J., Nicewander, W.A., 1988. Thirteen Ways to Look at the
1062 Correlation Coefficient. *The American Statistician* 42, 59–66. doi:10.
1063 1080/00031305.1988.10475524.

- 1064 Li, Y., Xia, C., 2000. Time-dependent tests on intact rocks in uniaxial
1065 compression. *International Journal of Rock Mechanics and Mining Sciences*
1066 37, 467–475. doi:10.1016/S1365-1609(99)00073-8.
- 1067 Maranini, E., Brignoli, M., 1999. Creep behaviour of a weak rock: exper-
1068 imental characterization. *International Journal of Rock Mechanics and*
1069 *Mining Sciences* 36, 127–138. doi:10.1016/S0148-9062(98)00171-5.
- 1070 Marsset, M., Carry, B., Dumas, C., Hanus, J., Viikinkoski, M., Vernazza, P.,
1071 Müller, T.G., Delbo, M., Jehin, E., Gillon, M., Grice, J., Yang, B., Fusco,
1072 T., Berthier, J., Sonnett, S., Kugel, F., Caron, J., Behrend, R., 2017. 3D
1073 shape of asteroid (6)~Hebe from VLT/SPHERE imaging: Implications for
1074 the origin of ordinary H chondrites. *Astronomy & Astrophysics* 604, A64.
1075 doi:10.1051/0004-6361/201731021, arXiv:1705.10515.
- 1076 Mazrouei, S., Daly, M., Barnouin, O., Ernst, C., DeSouza, I., 2014. Block
1077 distributions on itokawa. *Icarus* 229, 181–189. doi:10.1016/j.icarus.
1078 2013.11.010.
- 1079 Melenk, J., Babuška, I., 1996. The partition of unity finite element method:
1080 Basic theory and applications. *Computer Methods in Applied Mechan-*
1081 *ics and Engineering* 139, 289–314. doi:10.1016/S0045-7825(96)01087-0,
1082 arXiv:arXiv:1011.1669v3.
- 1083 Mellon, M.T., Feldman, W.C., Prettyman, T.H., 2004. The presence and
1084 stability of ground ice in the southern hemisphere of Mars. *Icarus* 169,
1085 324–340. doi:10.1016/j.icarus.2003.10.022.

- 1086 Melosh, H.J., 2011. Planetary Surface Processes. Cambridge University
1087 Press, Cambridge, UK New York. doi:10.1017/CB09780511977848.
- 1088 Merle, R., Dolbow, J., 2002. Solving thermal and phase change problems
1089 with the eXtended finite element method. Computational Mechanics 28,
1090 339–350. doi:10.1007/s00466-002-0298-y.
- 1091 Migliazza, M., Ferrero, A.M., Spagnoli, A., 2011. Experimental investigation
1092 on crack propagation in Carrara marble subjected to cyclic loads. Inter-
1093 national Journal of Rock Mechanics and Mining Sciences 48, 1038–1044.
1094 doi:10.1016/j.ijrmms.2011.06.016.
- 1095 Moës, N., Dolbow, J., Belytschko, T., 1999. A finite element method for crack
1096 growth without remeshing. International Journal for Numerical Methods
1097 in Engineering 46, 131–150.
- 1098 Molaro, J., Byrne, S., Le, J.L., 2017. Thermally induced stresses in boulders
1099 on airless body surfaces, and implications for rock breakdown. Icarus 294,
1100 247–261. doi:10.1016/j.icarus.2017.03.008.
- 1101 Murdoch, N., Sanchez, P., Schwartz, S.R., Miyamoto, H., 2015. Asteroid
1102 Surface Geophysics. Asteroids IV , 767–792doi:10.2458/azu_uapress_
1103 9780816532131-ch039, arXiv:1503.01931.
- 1104 Nash Gifford, L., Hilton, P.D., 1978. Stress intensity factors by enriched
1105 finite elements. Engineering Fracture Mechanics 10, 485–496. doi:10.
1106 1016/0013-7944(78)90059-0.
- 1107 Newman, J.C., 1971. An Improved Method of Collocation for the Stress Anal-
1108 ysis of Cracked Plates with Various Shaped Boundaries. NASA Technical

1109 Note, Langley Research Centre Hampton, Vu. 23365, National Aeronautics
1110 and Space Administration, Washington DC , 1–45.

1111 Opeil, C., Consolmagno, G., Britt, D., 2010. The thermal conductivity of
1112 meteorites: New measurements and analysis. *Icarus* 208, 449–454. doi:10.
1113 1016/j.icarus.2010.01.021.

1114 Opeil, C.P., Consolmagno, G.J., Safarik, D.J., Britt, D.T., 2012. Stony
1115 meteorite thermal properties and their relationship with meteorite chem-
1116 ical and physical states. *Meteoritics and Planetary Science* 47, 319–329.
1117 doi:10.1111/j.1945-5100.2012.01331.x.

1118 Paris, P., Tada, H., Donald, K., 1999. Service load fatigue damage - a
1119 historical perspective. *International Journal of Fatigue* 21, 35–46. doi:10.
1120 1016/S0142-1123(99)00054-7.

1121 Pettengill, G.H., Jurgens, R.F., 1979. Radar observations of asteroids. *As-
1122 teroids* 97, 206–211. doi:10.1086/131619.

1123 Ravaji, B., Ali-Lagoa, V., Delbo, M., Wilkerson, J., 2018. The effect of
1124 rotation period on thermal stress weathering, in: *Lunar and Planetary
1125 Science Conference*.

1126 Reddy, J.N.J.N., 2006. An introduction to the finite element method.
1127 McGraw-Hill Higher Education, New York, NY.

1128 Rhee, H., Salama, M.M., 1987. Mixed-mode stress intensity factor solutions
1129 of a warped surface flaw by three-dimensional finite element analysis. *En-
1130 gineering Fracture Mechanics* 28, 203–209. doi:10.1016/0013-7944(87)
1131 90214-1.

- 1132 Rice, J.R., 1968. A Path Independent Integral and the Approximate Anal-
1133 ysis of Strain Concentration by Notches and Cracks. *Journal of Applied*
1134 *Mechanics* 35, 379. doi:10.1115/1.3601206.
- 1135 Robinson, M.S., Thomas, P.C., Veverka, J., Murchie, S., Carcich, B., 2001.
1136 The nature of ponded deposits on Eros. *Nature* 413, 396–400. doi:10.
1137 1038/35096518.
- 1138 Rozitis, B., Green, S.F., 2011. Directional characteristics of thermal-infrared
1139 beaming from atmosphereless planetary surfaces - a new thermophysical
1140 model. *Monthly Notices of the Royal Astronomical Society* 415, 2042–2062.
1141 doi:10.1111/j.1365-2966.2011.18718.x.
- 1142 Rozitis, B., Green, S.F., MacLennan, E., Emery, J.P., 2018. Observing the
1143 variation of asteroid thermal inertia with heliocentric distance. *Monthly*
1144 *Notices of the Royal Astronomical Society* 477, 1782–1802. doi:10.1093/
1145 *mnras/sty640*.
- 1146 S. M. Beden, Abdullah, S., A. K. Ariffin, 2009. Review of Fatigue Crack
1147 Propagation Models for Metallic Components *Review of Fatigue Crack*
1148 *Propagation Models for Metallic Components*. *European Journal of Sci-*
1149 *entific Research* 28, 364–397.
- 1150 Saito, J., Miyamoto, H., Nakamura, R., Ishiguro, M., Michikami, T., Naka-
1151 mura, A.M., Demura, H., Sasaki, S., Hirata, N., Honda, C., Yamamoto, A.,
1152 Yokota, Y., Fuse, T., Yoshida, F., Tholen, D.J., Gaskell, R.W., Hashimoto,
1153 T., Kubota, T., Higuchi, Y., Nakamura, T., Smith, P., Hiraoka, K., Honda,
1154 T., Kobayashi, S., Furuya, M., Matsumoto, N., Nemoto, E., Yukishita,

- 1155 A., Kitazato, K., Dermawan, B., Sogame, A., Terazono, J., Shinohara,
1156 C., Akiyama, H., 2006. Detailed Images of Asteroid 25143 Itokawa from
1157 Hayabusa. *Science* 312, 1341–1344. doi:10.1126/science.1125722.
- 1158 Sankararaman, S., Ling, Y., Mahadevan, S., 2011. Uncertainty quantifica-
1159 tion and model validation of fatigue crack growth prediction. *Engineering*
1160 *Fracture Mechanics* 78, 1487–1504. doi:10.1016/j.engfracmech.2011.
1161 02.017.
- 1162 Smyth, J.R., 1975. High temperature crystal chemistry of fayalite. *American*
1163 *Mineralogist* 60, 1092–1097.
- 1164 Spencer, J.R., Lebofsky, L.A., Sykes, M.V., 1989. Systematic biases in ra-
1165 diometric diameter determinations. *Icarus* 78, 337–354. doi:10.1016/
1166 0019-1035(89)90182-6.
- 1167 Sun, C., Jin, Z.H., 2012. The Elastic Stress Field around a Crack Tip,
1168 in: *Fracture Mechanics*. Elsevier. chapter 3, pp. 25–75. doi:10.1016/
1169 B978-0-12-385001-0.00003-1.
- 1170 Tada, H., Paris, P.C., Irwin, G.R., 2000. *The Stress Analysis of Cracks*
1171 *Handbook, Third Edition*. Handbook, Del Research Corporation doi:10.
1172 1115/1.801535.
- 1173 Thomas, P.C., Veverka, J., Robinson, M.S., Murchie, S., 2001. Shoemaker
1174 crater as the source of most ejecta blocks on the asteroid 433 Eros. *Nature*
1175 413, 394–396. doi:10.1038/35096513.
- 1176 Veverka, J., Farquhar, B., Robinson, M., Thomas, P., et al., 2001a. The

- 1177 landing of the NEAR-Shoemaker spacecraft on asteroid 433 Eros. *Nature*
1178 413, 390–393. doi:10.1038/35096507.
- 1179 Veverka, J., Thomas, P.C., Robinson, M., Murchie, S., et al., 2001b. Imaging
1180 of small-scale features on 433 Eros from NEAR: evidence for a complex
1181 regolith. *Science (New York, N.Y.)* 292, 484–8. doi:10.1126/science.
1182 1058651.
- 1183 Walsh, K.J., Jawin, E.R., Ballouz, R.L., Barnouin, O.S., 2019. Craters,
1184 boulders and regolith of (101955) bennu indicative of an old and dynamic
1185 surface. in press, *Nature Geoscience* .
- 1186 Wilkins, B., 1980. Slow crack growth and delayed failure of granite. *Inter-*
1187 *national Journal of Rock Mechanics and Mining Sciences & Geomechanics*
1188 *Abstracts* 17, 365–369. doi:10.1016/0148-9062(80)90520-3.
- 1189 Williams, M.L., 1961. The Bending Stress Distribution at the Base of a
1190 Stationary Crack. *Journal of Applied Mechanics* 28, 78. doi:10.1115/1.
1191 3640470.
- 1192 Wilson, W.K., Yu, I.W., 1979. The use of the J-integral in thermal stress
1193 crack problems. *International Journal of Fracture* 15, 377–387. doi:10.
1194 1007/BF00033062.
- 1195 Witkowski, T., Ling, S., Praetorius, S., Voigt, A., 2015. Software concepts
1196 and numerical algorithms for a scalable adaptive parallel finite element
1197 method. *Advances in Computational Mathematics* 41, 1145–1177. doi:10.
1198 1007/s10444-015-9405-4.

1199 Yau, J.F., Wang, S.S., Corten, H.T., 1980. A Mixed-Mode Crack Analysis of
1200 Isotropic Solids Using Conservation Laws of Elasticity. *Journal of Applied*
1201 *Mechanics* 47, 335. doi:10.1115/1.3153665.